Single nucleosome imaging reveals loose genome chromatin networks via active RNA polymerase II

永島　崚甫

博士（理学）

総合研究大学院大学
生命科学研究科
遺伝学専攻

平成３０（２０１８）年度

Single nucleosome imaging reveals loose genome chromatin networks via active RNA polymerase II

Nagashima, Ryosuke

Doctor of Philosophy

Department of Genetics

School of Life Science

SOKENDAI

(Graduate University for Advanced Studies)

2018 (school year)

Contents

List of Figures

Abstract

In our body, 2 m of genomic DNA, which encodes genetic information, is packaged in the cell nucleus with a diameter of ~10 μm. The long stranded DNA is wrapped around histone octamers to form nucleosomes and three-dimensionally organized in the cells as chromatin. In the process of information output (gene transcription), which specifies cellular function and subsequent fates, both chromatin organization and dynamics play a critical role in governing accessibility to genomic information. Generally, people think that transcribed chromatin regions are more open and dynamic. Contrary to this general view, however, we previously revealed that transcriptional inhibition by an inhibitor 5, 6-Dichloro-1-β-D -ribofuranosyl benzimidazole (DRB) treatment globally upregulated the chromatin movements in whole nucleus in living human cells. This suggested that transcriptional process globally constrained the chromatin dynamics. In this thesis, I investigated the mechanism how the chromatin dynamics is globally constrained by transcription. For this purpose, I performed single nucleosome imaging under several conditions that affect global transcription by inhibitor treatments of RNA polymerase II (RNAPII), RNAPII rapid depletion, and serum starvation to enter the cells into quiescent (G0) state.

To measure the chromatin dynamics, I established a human RPE-1 cell line stably expressing histone H2B tagged with HaloTag and performed single nucleosome imaging. At first, to examine the role of the transcriptional process in constraint of chromatin motion, I treated the RPE-1 cells with DRB or α-amanitin (α-AM). Both inhibitors are known to reduce active RNAPII on chromatin. Indeed, both inhibitor treatments significantly reduced the amount of active RNAPII and globally upregulated chromatin

dynamics, as consistent with our previous report. Based on these results, I hypothesized that active RNAPIIs on chromatin restricted the chromatin dynamics.

To test this hypothesis, I examined the effect of another inhibitor, actinomycin D (ActD), which induces stalling of active RNAPII on chromatin. While ActD treatment reduced global RNA synthesis in the cells, the amounts of active RNAPII marks in the treated cells were similar or slightly higher than those of untreated control cells, suggesting more active RNAPIIs on the chromatin. In contrast to the DRB and α-AM results, ActD treatment decreased the chromatin dynamics and induced more chromatin constraints. This result supported that the active RNAPII complexes on chromatin constrained the chromatin movements.

To demonstrate the involvement of RNAPII in the chromatin constraints more directly, I generated DLD-1 cells that enable me to perform rapid and specific degradation of RPB1, the largest subunit of RNAPII, by an auxin-inducible degron (AID) system. The DLD-1 cells were also expressing H2B-HaloTag. In the established cells, RPB1 was rapidly depleted within one hour after auxin addition and the chromatin dynamics was significantly increased. This result strengthened my hypothesis that RNAPII directly constrains chromatin movements.

Furthermore, to investigate chromatin constraints by active RNAPII in a more physiological state, I induced the RPE-1 cells into a transcriptionally-less-active G0 state by serum removal from the culture medium. G0 entry was confirmed by loss of the proliferation markers Ki67 or Topoisomerase IIα in the treated cells. I showed the G0-

induced cells increased the chromatin dynamics and decreased active RNAPIIs, as compared with untreated control cells. In addition, one day after serum restoration into medium, the cells became Ki67 positive and suppressed chromatin movements. Concurring with this chromatin dynamics decreased, active RNAPII marks were restored in the serum re-added cells. Taken together, these results revealed chromatin constraints by active RNAPII in physiological context.

Using single nucleosome imaging, I investigated genome-wide chromatin dynamics in a whole nucleus of living human cells, and demonstrated the constraints on chromatin movements via active RNAPII. What is the underling molecular mechanism for globally constraining chromatin motion? Related to this issue, it has been long proposed that stable clusters of RNAPII work as transcription factories and immobilize chromatin to be transcribed. Recent studies have also shown that active RNAPII and P-TEFb complex consisting of Cyclin T1 (CYCT1) and CDK9 kinase, which interact with RNAPII, form clusters in living cells. Based on the available and obtained data, I consider the following model: Transcription complex/clusters including active RNAPII weakly connect multiple chromatin domains for a loose spatial genome chromatin network. Chromatin is thus globally stabilized or constrained by the loose network. In this model, P-TEFb clusters work as “hubs” and active RNAPIIs working on the cluster work as “glues” for the multiple weak interactions in the network. Consistent with this, knockdown of CDK9 by siRNA upregulated chromatin movements upon reduction of CDK9 protein levels in the RPE-1 cells.

Introduction

Genomic DNA, which encodes genetic information, is spatially and temporally organized in the cell as chromatin (Bickmore, 2013; Cardoso et al., 2012; Dekker and Heard, 2015; Hubner et al., 2013). In the process of information output (gene transcription), which specifies cellular function and subsequent fates, both chromatin organization and dynamics play a critical role in governing accessibility to genomic information. Emerging evidence reveals that the nucleosomes (10-nm fibers), consisting of genomic DNA wrapped around the core histones (Luger et al., 1997), seem to be folded rather irregularly (Chen et al., 2016; Eltsov et al., 2008; Fussner et al., 2012; Hsieh et al., 2015; Maeshima et al., 2016; Ou et al., 2017; Ricci et al., 2015; Risca et al., 2017; Sanborn et al., 2015). This implies that the chromatin is less physically constrained and more dynamic than expected in the regular static structures model (Maeshima et al., 2010a). Consistently, live cell imaging studies have long revealed a highly dynamic nature of chromatin using LacO/LacI-GFP and related systems (Chubb et al., 2002; Germier et al., 2017; Hajjoul et al., 2013; Heun et al., 2001; Levi et al., 2005 ; Marshall et al., 1997), and more recently, single nucleosome imaging (Hihara et al., 2012; Nozaki et al., 2017) and CRISPR/dCas9-based strategies (Chen et al., 2013; Gu et al., 2018; Ma et al., 2016).

Regarding larger-scale chromatin organization, several models have been proposed, for example, chromonema fibers (Belmont and Bruce, 1994; Hu et al., 2009 ; Kireeva et al., 2004) or nucleosome clusters/domains (Nozaki et al., 2017) with a diameter of 100–200 nm, and globular DNA replication foci/domains with an average diameter of 110–150 nm observed via fluorescent pulse labeling (Albiez et al., 2006; Baddeley et al., 2010; Berezney et al., 2000; Cseresnyes et al., 2009; Jackson and Pombo, 1998; Markaki et al.,

2010; Xiang et al., 2018). Recently chromosome conformation capture (3C) and related methods including Hi-C (Lieberman-Aiden et al., 2009) have enabled the production of a fine contact probability map of genomic DNA and supported the formation of numerous chromatin domains, designated as topologically associating domains (TADs) (Dekker and Heard, 2015; Dixon et al., 2012; Nagano et al., 2017; Nora et al., 2012; Sexton et al., 2012; Smallwood and Ren, 2013; Szabo et al., 2018), and more recently contact domains/loop domains (Eagen et al., 2015; Rao et al., 2014; Rao et al., 2017; Vian et al., 2018), which are considered functional units of the genome with different epigenetic features. These contact probability maps have also suggested various intra-chromosomal and inter-chromosomal domain contacts for global control of gene transcription (Dekker and Heard, 2015; Dixon et al., 2012; Eagen et al., 2015; Nagano et al., 2017; Nora et al., 2012; Rao et al., 2014; Sexton et al., 2012; Smallwood and Ren, 2013), although the underlying mechanism remains unclear.

An interesting observation, which might explain the relationship between global chromatin behavior and gene transcription, came from single nucleosome imaging to see local chromatin movements in a whole nucleus of 2D-focal plane in human cells treated with RNA polymerase II (RNAPII) inhibitor (5,6-Dichloro-1-β-D-ribofuranosyl benzimidazole; DRB) (Kwak and Lis, 2013). Contrary to the general view that transcribed chromatin regions are more open and dynamic, the inhibitor treatment globally upregulated the chromatin dynamics (Nozaki et al., 2017). While recent studies reported that some specific genomic loci in human breast cancer and mouse embryonic stem cells became less dynamic when actively transcribed (Germier et al., 2017; Ochiai et al., 2015), the transcribed chromatin regions in the whole genome are very limited in human cells

(Djebali et al., 2012). Then how can transcription globally affect chromatin dynamics? Related to this issue, it has been long proposed that stable clusters of RNAPII work as transcription factories and immobilize the chromatin to be transcribed (Buckley and Lis, 2014; Feuerborn and Cook, 2015). Recent single molecule tracking studies have also shown that active RNAPII and other factors form transient and dynamic clusters (Cho et al., 2016; Cho et al., 2018; Chong et al., 2018; Cisse et al., 2013). Taken together, I hypothesized that chromatin domains form loose network via transcription complexes for efficient gene transcription and that chromatin is globally stabilized or constrained by such a network. I inferred that inhibition or removal of RNAPII can disrupt the network connections and increase chromatin movements.

To test this hypothesis, using single nucleosome imaging (Hihara et al., 2012; Nozaki et al., 2017), I investigated genome-wide chromatin dynamics in a whole nucleus in living human RPE-1 cells treated with various transcriptional inhibitions. I found that treatments of RNAPII inhibitors, DRB and α-amanitin, globally raised the chromatin fluctuation, suggesting less constraints of chromatin movements. A conditional rapid depletion of RNAPII had a similar effect. Furthermore, the chromatin mobility increased in quiescent G0 phase cells with serum starvation, which are less transcriptionally active. My imaging results suggest that chromatin is globally stabilized by loose connections through transcriptionally active RNAPII. Taken together with available data, I infer the existence of loose chromatin domain networks for various intra-chromosomal and inter-chromosomal contacts via transient clustering of active RNAPII.

Results

Single nucleosome imaging in human RPE-1 cells

I performed single nucleosome imaging to accurately measure local chromatin dynamics in a whole nucleus and to get a clue on chromatin organization. For the imaging, a H2B-HaloTag (H2B-Halo) transgene was stably expressed in RPE-1 cells, which is a retinal pigment epithelial cell line immortalized by hTERT (Bodnar et al., 1998) (Figure 1). To label the H2B-Halo, a HaloTag ligand TMR (Tetramethylryodamine) which can bind specifically to a HaloTag in living cells was used. The HaloTag-fused histone H2B is incorporated into the nucleosomes throughout the genome including euchromatic and heterochromatic regions (Figure 2), presumably by histone replacement on a scale of hours (Kimura and Cook, 2001). Stepwise salt washing of nuclei isolated from the established H2B-Halo-expressing cells confirmed that H2B-Halo behaved similar to the endogenous H2B (Figure 3), suggesting that the H2B-Halo molecules were incorporated properly into the nucleosomes in these cells. For single nucleosome imaging, I used oblique illumination microscopy, which allowed me to illuminate a thin area within a single nucleus with reduced background noise (green line in Figure 4; Nozaki et al., 2017; Tokunaga et al., 2008). Prior to imaging, H2B-Halo molecules were labeled with low concentration of TMR (Figure 5) to produce a relatively small number [~100-200/time frame (50 ms)/nucleus] of fluorescent nucleosomes containing H2B-Halo. Clear and well-separated dots were detected (Figure 6), with a single-step photobleaching profile (Figure 7), which suggested that each dot represents a single H2B-Halo-TMR molecule in a single nucleosome. The TMR dye has higher intensity and 10 times longer life time before photobleach than those of PA-mCherry (Subach et al., 2009) that our laboratory previously used (Nozaki et al., 2017). Both of these characteristics of the TMR

contributed to improve single nucleosome imaging.

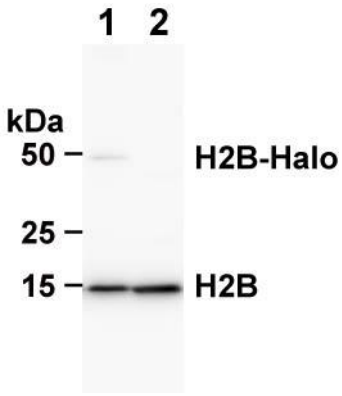

Figure 1. Immunoblotting against for H2B protein.
Expression of H2B-HaloTag (H2B-Halo) in RPE-1 cells was confirmed by Immunoblotting with anti-H2B antibody (Lane 1). In Lane 2, parental RPE-1 cells shows no H2B-Halo signals.

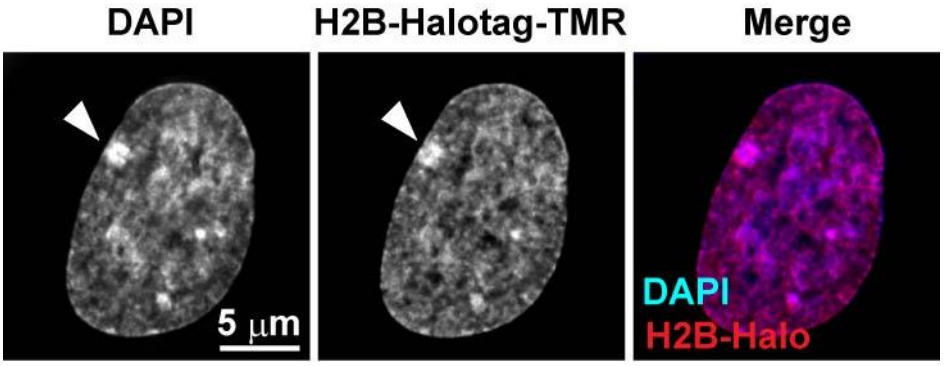

Figure 2. HaloTag ligand staining on H2B-Halo expressing RPE-1 cell.
A image of RPE-1 cell expressing H2B-Halo which was fluorescently labeled with TMR-HaloTag ligand (center). The left panel is DNA stained with DAPI. The merged image (DNA, blue; H2B-Halo, red) is shown at right. Putative inactive X chromosome, which is highly condensed, is marked with an arrow head. Note that the TMR labeling pattern is very similar to DNA staining one.

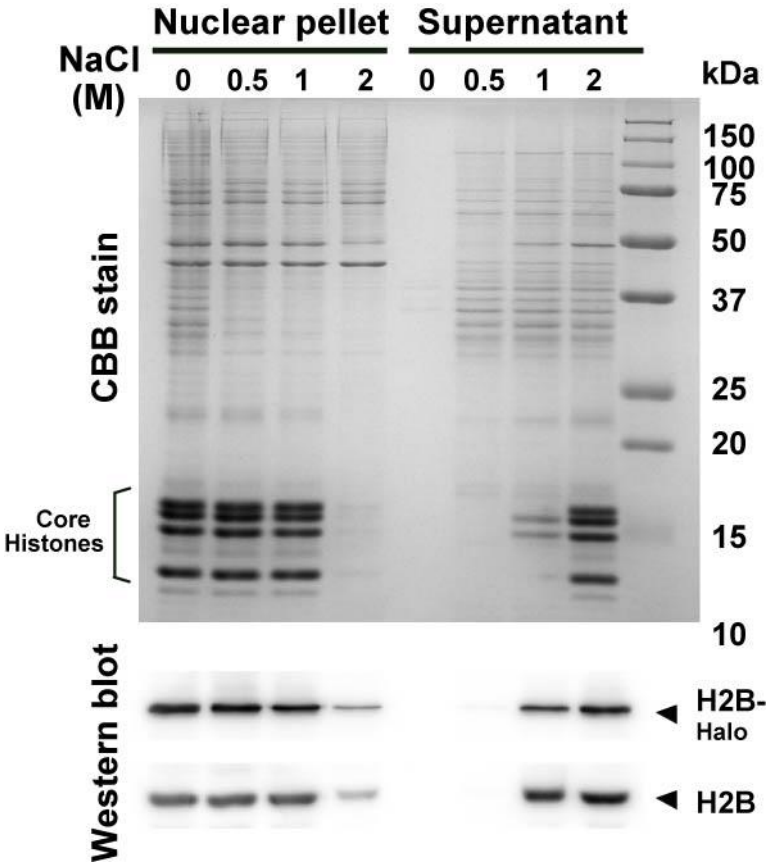

Figure 3. CBB staining and immunoblotting against for H2B protein regarding nuclei of H2B-Halo expressing RPE-1 cells which were biochemically fractionated.

The nuclei isolated from the RPE-1 cells expressing H2B-Halo were washed with the indicated buffers including various concentrations of NaCl. The resultant nuclear pellets (left) and supernatants (right) were analyzed by SDS-PAGE, and subsequent CBB staining (upper) and Western blotting (bottom) with anti-H2B antibodies. Note that H2B and H2B-Halo started to dissociate from chromatin with 1 M NaCl and were detected in the supernatant fraction, suggesting that H2B-Halo was incorporated into nucleosome structures similar to endogenous H2B.

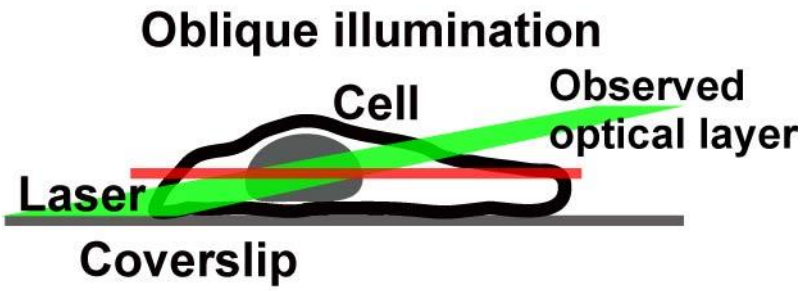

Figure 4. Scheme of oblique illumination.

This illumination laser (green) can excite fluorescent molecules within a limited thin optical layer (red) of the nucleus and reduce background noise.

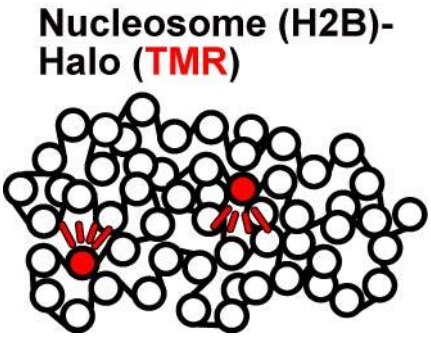

Figure 5. Scheme of TMR-labeled nucleosomes.

A small fraction of H2B-Halo was fluorescently labeled with TMR-HaloTag ligand (red).

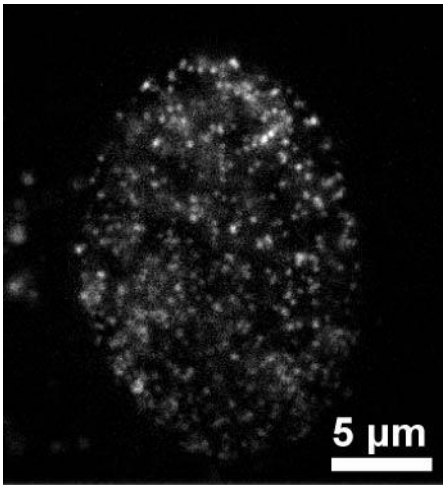

Figure 6. A single-nucleosome [H2B-Halo-TMR] image of a living RPE-1 nucleus.

Each bright dot represents single-nucleosome. Scale bar is 5 µm.

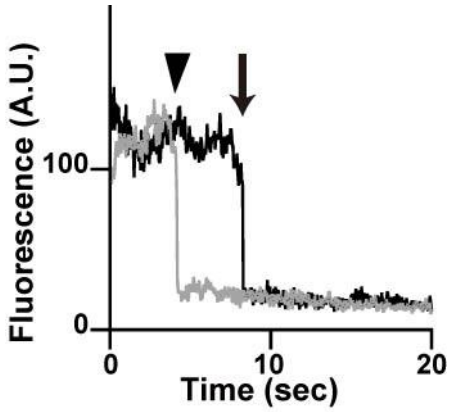

Figure 7. Single-step photobleaching of two representative nucleosome [H2B-Halo-TMR] dots.
The vertical axis represents the fluorescence intensity of individual TMR dots. The horizontal axis is the tracking time series. The fluorescent intensity of each dot was approximately 120, and in the single-step photobleaching profile, the intensity dropped to around 10 (arrowhead and arrow), suggesting that each dot represents a single H2B-Halo-TMR molecule in a single nucleosome.

I recorded the TMR-labeled nucleosome dots in the interphase chromatin at 50 ms/frame (~100 frames, 5 s total) in living cells. The individual dots were fitted with a 2D Gaussian function to estimate the precise position of the nucleosome (the position determination accuracy is 15.55 nm; Figure 8; Betzig et al., 2006; Rust et al., 2006; Selvin et al., 2007). I first tracked each nucleosome movement using u-track software (Figure 9; Jaqaman et al., 2008). Notably, I tracked only signals of H2B-Halo-TMR incorporated into nucleosomes since free histones moved too fast to detect as dots and track under my imaging conditions. Effects of nuclear movements were negligible in my conditions. The plots of calculated mean square displacement (MSD) were well fitted to a subdiffusion model (black line in Figure 10), which is in a good agreement with those of H2B-PA-mCherry similarly expressed in RPE-1 cells (gray line in Figure 10; Figure 11; Figure 12; Figure 13). Chemical fixation of the cells with formaldehyde (FA) to crosslink

nucleosomes severely suppressed the movements of TMR-nucleosomes (red line in Figure 10), indicating that most of the observed movement was derived from real nucleosome movements in living cells. When I analyzed the nucleosome movements within a longer time window, the MSD almost reaches to a plateau (p) (Figure 14), which is proportional to the square the radius of constraint (Rc; $p = 6/5 \times Rc^2$) (Dion and Gasser, 2013). The estimated radius of constraint (Rc) of the nucleosome motion in living cells is about 144 nm while that of nucleosomes in FA-fixed cells is about 56 nm. Spatial distributions of the obtained nucleosome movements were also visualized as a "chromatin heatmap" in the nucleus: larger chromatin movement appears as more "red" (or hot), and smaller movement appears as more "blue" (or cold) pixels (Figure 15).

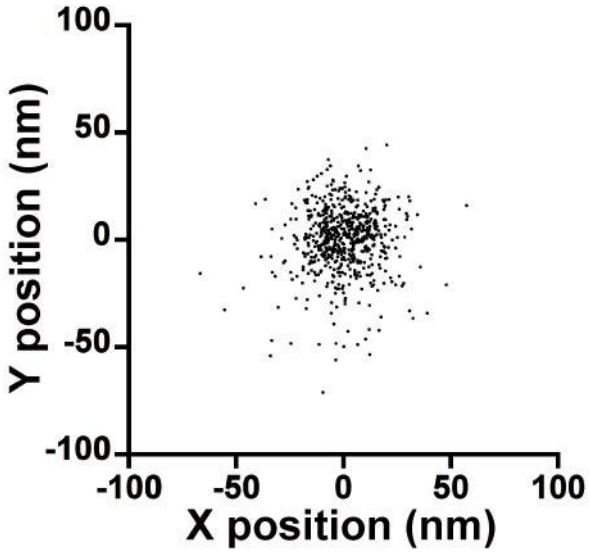

Figure 8. The position determination accuracy of Halotag ligand TMR labeled H2B-Halo proteins. Distribution of nucleosome displacements from centroid of their localizations in the x-y plane in the 50 ms interval. n = 10 nucleosomes in a formaldehyde (FA)-fixed cell. Standard deviations (SD_x and SD_y) were 13.4 nm and 15.1 nm, respectively.

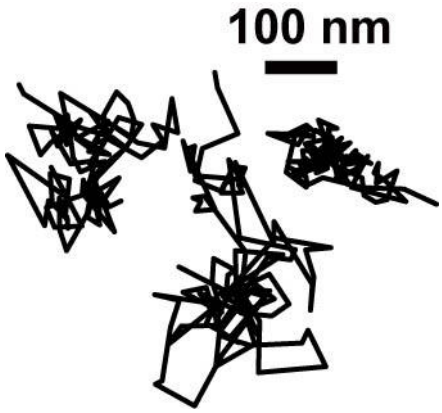

Figure 9. Trajectories of nucleosomes.

Representative 3 trajectories of the tracked single nucleosomes. Bar, 100 nm.

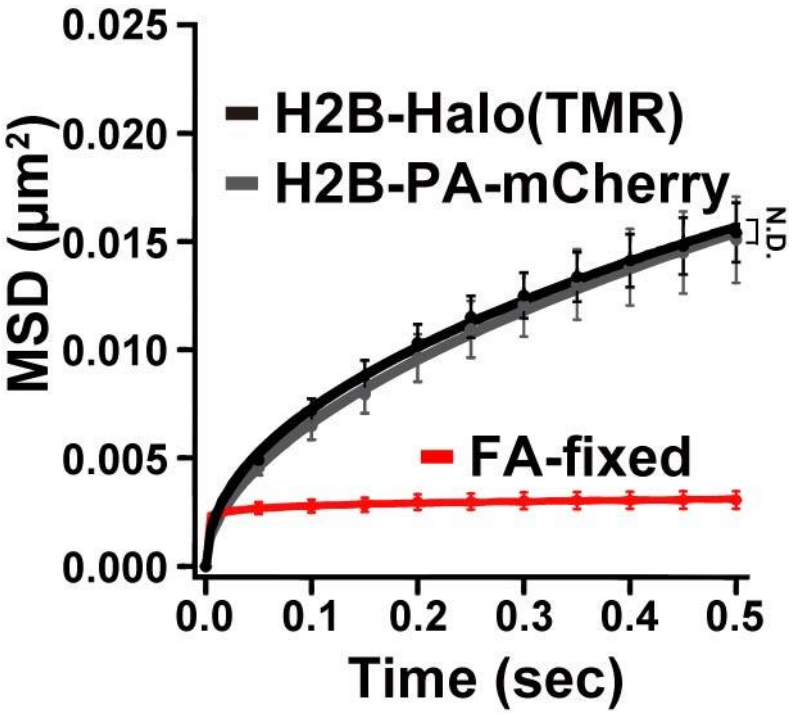

Figure 10. Mean square displacement plots of single nucleosomes in RPE-1 cells.

Mean square displacement (MSD) plots (± standard deviation [s.d.] among cells) of single nucleosomes in living interphase (black) and formaldehyde (FA)-fixed (red) RPE-1 cells from 0.05 to 0.5 s. For comparison, MSD plots of single nucleosomes labeled with PA-mCherry (H2B-PA-mCherry) in living interphase RPE-1 cells (gray) are also shown. For each sample, n = 20–25 cells. N.D. means not detected, Kolmogorov–Smirnov test for H2B-Halo versus H2B-PA-mCherry ($p = 0.47$). In the MSD analyses for single nucleosomes, the originally calculated MSD was in two dimensions. To obtain three-dimensional values, the original values of MSD were multiplied by 1.5 (4Dt to 6Dt). The plots were fitted as a subdiffusion curve.

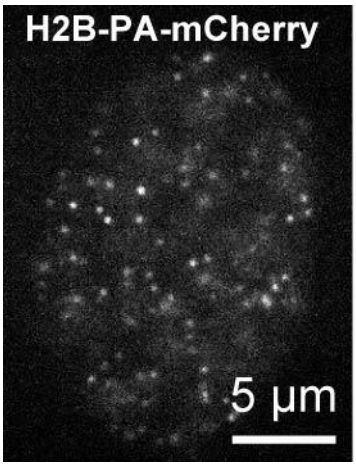

Figure 11. A single-nucleosome [H2B-PA-mCherry] image of a living RPE-1 nucleus.
Each bright dot represents single H2B-PA-mCherry protein. Bar, 5 μm.

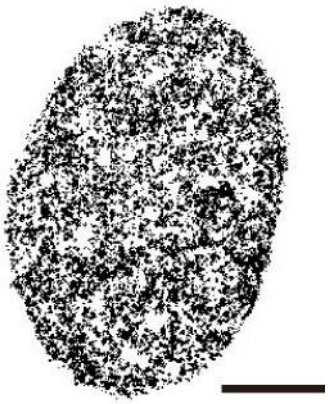

Figure 12. A photoactivated localization microscopy (PALM) image of H2B-PA-mCherry protein.
Live-cell PALM image of histone H2B of the same cell in Figure 11. Bar, 5 μm.

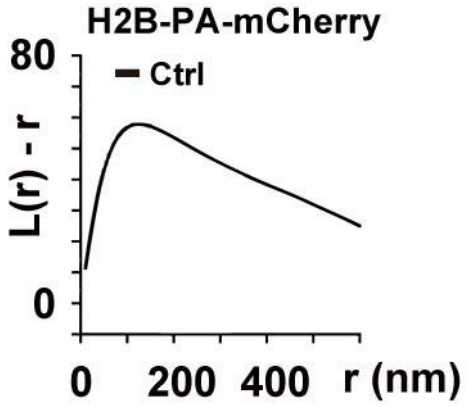

Figure 13. The L-function plot of live RPE-1 cells expressing H2B-PA-mCherry.

The L-function plot shows a curve with a peak at ~120 nm (i.e., ~240 nm in diameter). This peak size, which can provide a good approximations of the size and compaction state of the domains, is consistent with a previous reported domain size in HeLaS3 cells (Nozaki et al., 2017). Shown is a representative image among ten PALM images.

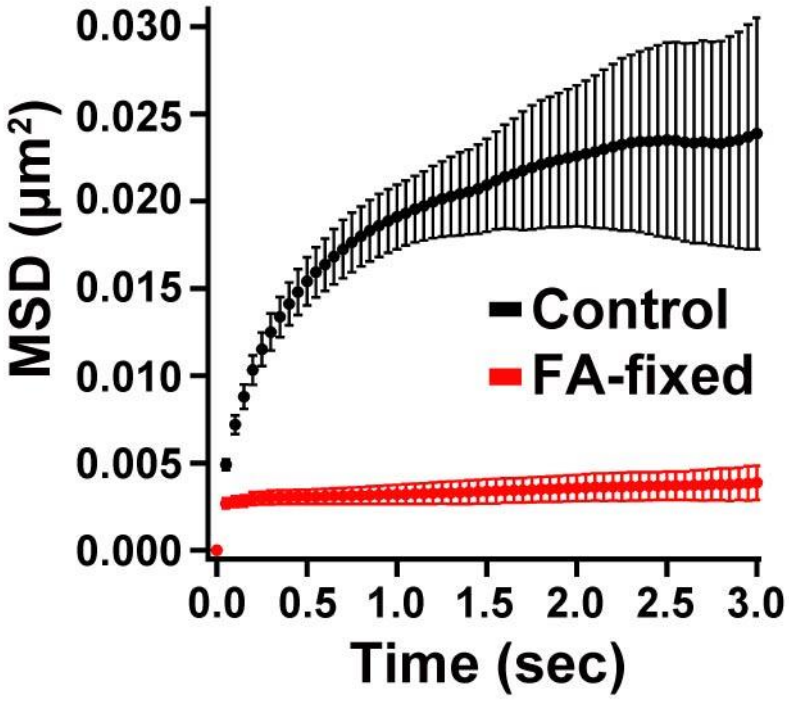

Figure 14. Long term MSD plots of single nucleosomes in H2B-Halo expressing RPE-1 cells.

MSD plots (± s.d. among cells) of single nucleosomes in living (black) and formaldehyde (FA)-fixed (red) RPE-1 cells in a long time range from 0.05 to 3 s. For each sample, n = 20–25 cells.

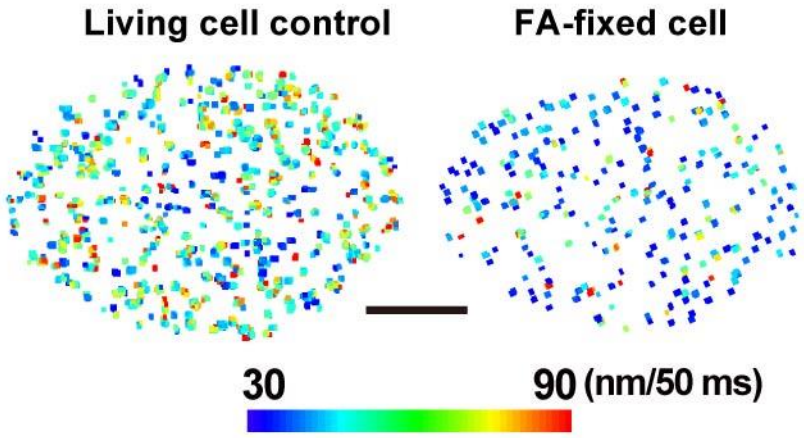

Figure 15. Chromatin heatmaps of RPE-1 cells.
(Left) Chromatin heatmap of the living RPE-1 cell: nucleosome movements for 50 msec. The color bar represents the scale of nucleosome movement in the heatmap. Small movements are shown in blue, and large movements are shown in red. (Right) The heatmap of a FA-fixed nucleus. Bar, 5 μm.

Transcriptional inhibition by DRB or α-amanitin diminished constraints of local chromatin movements

To examine the role of the transcriptional process in constraint of chromatin motion, I first treated cells with DRB or α-amanitin (α-AM). DRB is a selective inhibitor of CDK9 kinase in the P-TEFb complex that phosphorylates Ser2 in C-terminal domain (CTD) of the largest subunit of RNAPII, RPB1, in eukaryotic cells and inhibits transcription elongation process (Figure 16) (Bensaude, 2011; Kwak and Lis, 2013). It was also reported that DRB caused dissociation of the RNAPII elongation complex from chromatin (Kimura et al, 2002). α-AM binds with high specificity and high affinity (Kd = 3–4 nM) near the catalytic active site of RNAPII (Bushnell et al., 2002) and induces degradation of the RPB1 (Nguyen et al., 1996). Immunostaining of two active RNAPII

markers, phosphorylated serine 5 (Ser5P) and serine 2 (Ser2P) of CTD (Stasevich et al., 2014), which are known to be involved in initiation and elongation process of RNAPII, respectively (Figure 16), showed punctate foci throughout nucleoplasm in untreated control (Figure 17; Figure 18; Figure 19). Note that in this thesis, I used the term "active RNAPII" as the one that has phosphorylated Ser5 or/and phosphorylated Ser2 and engages in transcriptional process (initiation or elongation). Both inhibitors treatments significantly reduced the amount of the two active RNAPII marks (Figure 17 and Figure 18). Consistently, these treatments markedly suppressed global RNA synthesis in the cells, which were measured by incorporation of a ribonucleotide analog, 5-ethynyl uridine (EU) (Figure 20). In these cells treated with DRB or α-AM, the local chromatin movement was globally upregulated (Figure 21 and Figure 22), as consistent with the chromatin heatmap (Figure 23) and our previous report (Nozaki et al., 2017). Interestingly, when the effects of DRB and α-AM were compared, I found that the amount of RNAPII-Ser5P seemed to be well correlated with constraints of chromatin movements (Figure 17; Figure 18; Figure 21; also see discussion). With MSD analysis within the longer time window (Figure 24), I estimated that Rc of the nucleosome motion in the cells treated with DRB or α-AM increased from 144 nm (control) to 156 nm or 170 nm, respectively, suggesting reduction in constraints. On the other hand, an RNA polymerase I Inhibitor CX-5461, which suppressed rRNA synthesis in nucleoli (Left, Figure 25) (Drygin et al., 2011), had almost no effect on the local chromatin dynamics (Right, Figure 25). Furthermore, inhibition of RNA splicing complex, which is associated with active RNAPII during its elongation process, by Pladienolide B (Koga et al., 2015) only slightly effected the chromatin dynamics (Left, Figure 26) although pre-mRNA production was almost normal and subsequent splicing process was severely inhibited by the inhibitor treatment (Right,

Figure 26). Taken together, these results suggested a specific role of the active RNAPII in restricting chromatin dynamics.

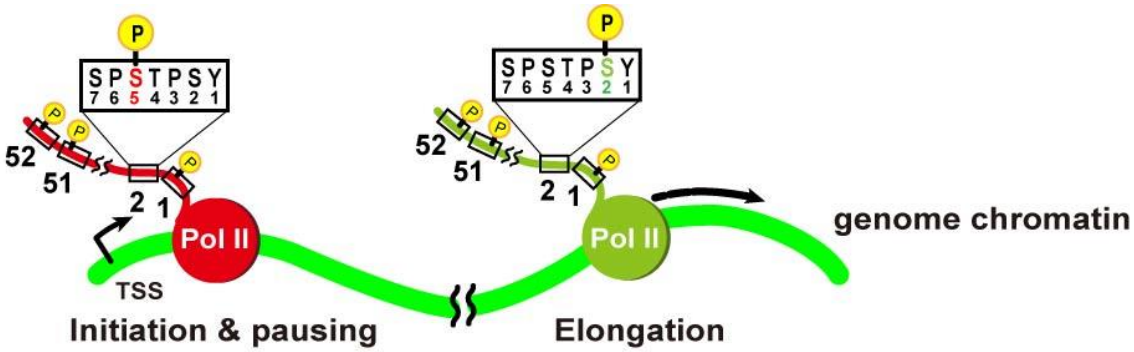

Figure 16. Scheme for RNAPII regulation by phosphorylations of its CTD repeats, (YSPTSPS) × 52. In the initiation process, RNAPII, in which Ser5 of CTD are phosphorylated, stays around initiation site (red, RNAPII-Ser5P) on the template DNA. For elongation, with phosphorylation of Ser2 of CTD, RNAPII complex goes along the template DNA (green, RNAPII-Ser2P)

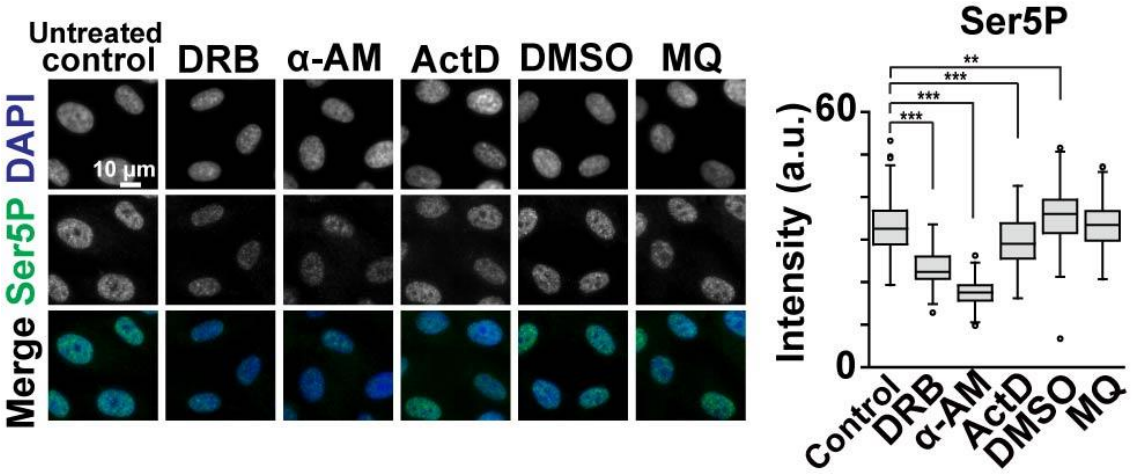

Figure 17. Immunostaining for phosphorylated serine 5 of CTD in transcription inhibitor treated cells. (Left) RNAPII activity in RPE-1 cells was monitored by immunostaining of active RNAPII marker (Stasevich et al., 2014), phosphorylated serine 5 (Ser5P) of RNAPII CTD. The inhibitors used were α-amanitin (α-AM), 5,6-dichlorobenzimidazole-1-β-D-ribofuranoside (DRB), Actinomycin D (ActD). As solvent control, dimethyl sulfoxide (DMSO) and ultrapure water (MQ) were used. First row, DNA staining with DAPI; second row, immunostaining of Ser5P of RNAPII CTD; third row, merged images. (Right) The quantification of RNAPII-Ser5P signal intensity is shown as box plot. The median intensities of Ser5P are 32.6 (n=118 cells) in control, 22.4 (n = 121 cells) in DRB, 17.5 (n = 141 cells) in α-AM, and 29.0 (n = 130 cells) in ActD. Bar, 10 µm. **p < 0.001, ***p < 0.0001, Wilcoxon signed-rank test for control versus DRB ($p < 2.2 \times 10^{-16}$) and for control versus α-AM ($p < 2.2 \times 10^{-16}$) and for control versus ActD ($p = 7.1 \times 10^{-5}$).

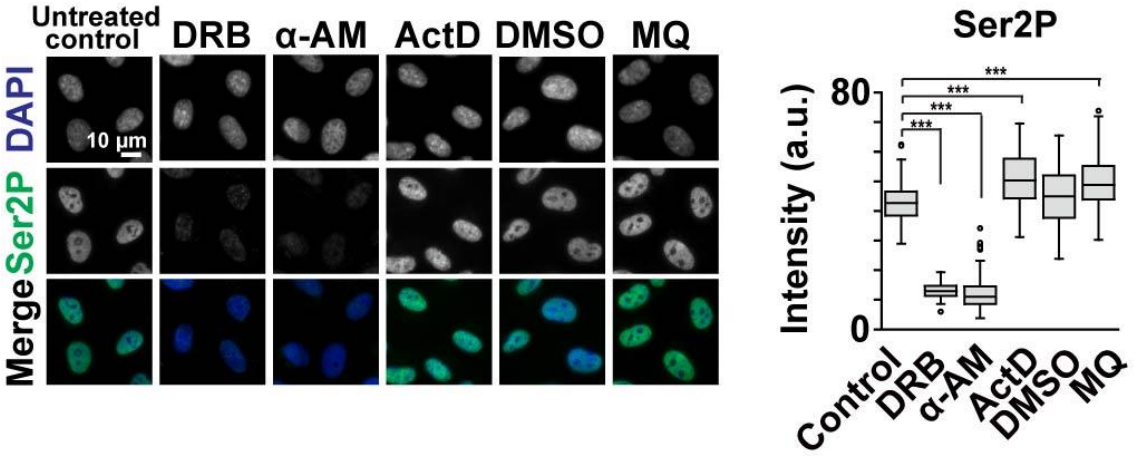

Figure 18. Immunostaining for phosphorylated serine 2 of CTD in transcription inhibitor treated cells. (Left) RNAPII activity, which was observed by immunostaining of Ser2P, in the RPE-1 cells treated with RNAPII inhibitors (DRB, α-AM, and ActD) or without them (Untreated control, DMSO, and MQ). (Right) Quantification of RNAPII Ser2P signal intensity, which is an indication of RNAPII elongation, is shown as a box plot. The median intensities of Ser2P are 42.7 (n = 114) in control, 12.9 (n = 119) in DRB, 11.1 (n = 129) in α-AM, and 50.3 (n = 123) in ActD. Note that the inhibitor treatments decreased the phosphorylation level at the serine 2, except for ActD. Bar, 10 μm. ***$p < 0.0001$, Wilcoxon signed-rank test for control versus DRB ($p < 2.2 \times 10^{-16}$) and for control versus α-AM ($p < 2.2 \times 10^{-16}$) and for control versus ActD ($p = 5.9 \times 10^{-11}$) and for control versus MQ ($p = 7.8 \times 10^{-10}$).

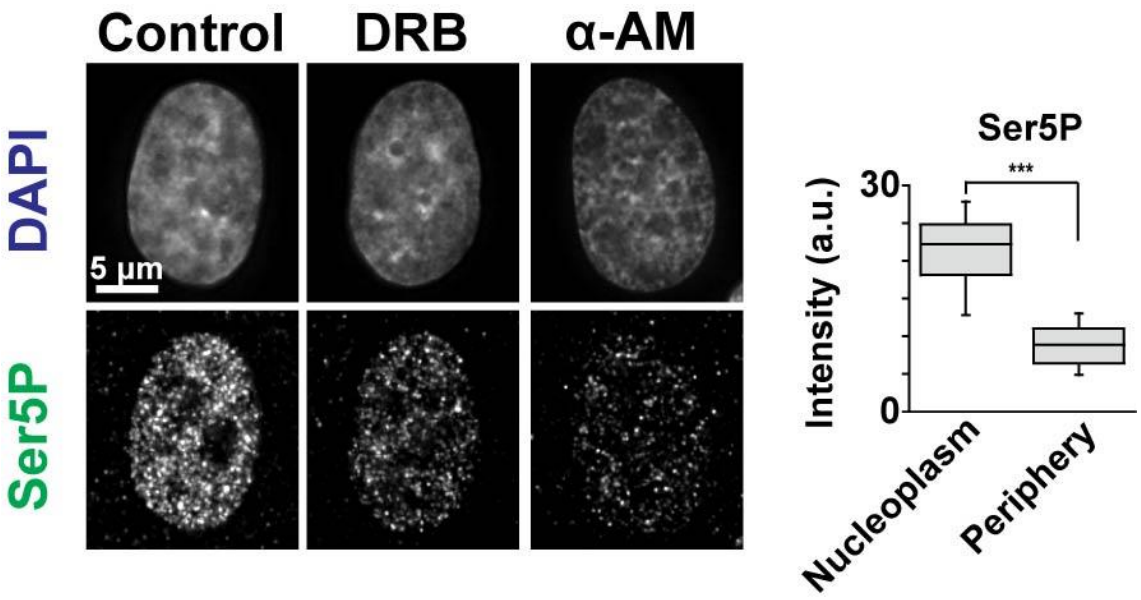

Figure 19. Distribution of RNAPII-Ser5P.

(Left) Active RNAPII (Ser5P) distribution in RPE-1 cells with DRB, α-AM or without inhibitors (Untreated control) observed by immunostaining. Typical images with deconvolution by DeltaVision softworx software are shown. RNAPII-Ser5P formed clusters and distributed in nucleoplasm except for nuclear periphery and nucleoli. (Right) Quantitative analysis of the nuclear periphery in the control shows that Ser5P is drastically reduced in the regions compared with nucleoplasm. ***$p < 0.0001$, Wilcoxon signed-rank test ($p = 1.1 \times 10^{-10}$).

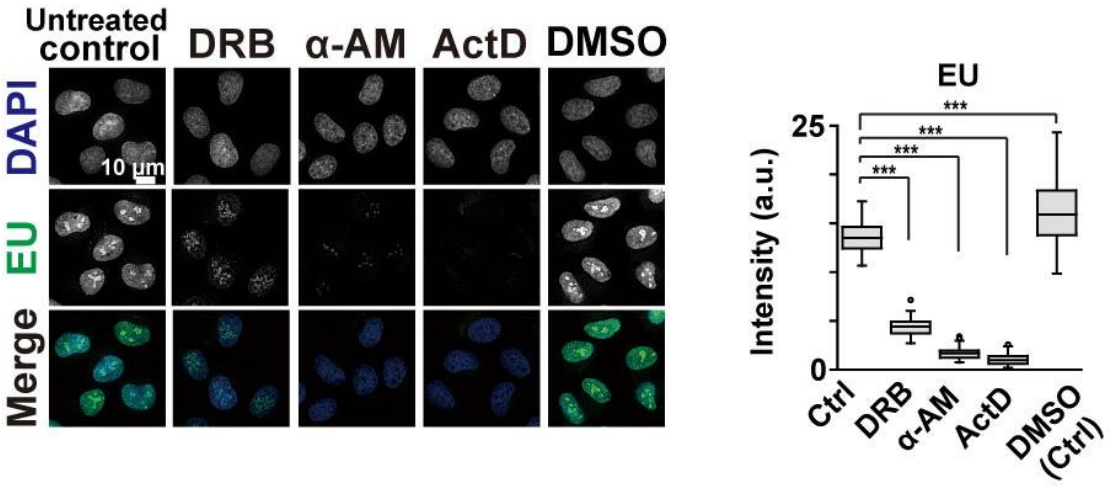

Figure 20. Verification of RNA synthesis inhibition with 5-ethynyl uridine (EU) incorporation.
(Left) Verification of RNA synthesis inhibition by RNAPII inhibitors (α-AM, DRB, and ActD) with 5-ethynyl uridine (EU) incorporation into RNA. The incorporated EU was detected with Alexa594-labeling by click chemistry. (Right) The quantification of EU signal intensity is shown as box plot. The median intensities of EU are 13.5 (n = 49 cells) in control, 4.44 (n = 48 cells) in DRB, 1.69 (n = 45 cells) in α-AM, 0.975 (n = 45 cells) in ActD, and 16.1 (n = 53 cells) in DMSO. Note that the inhibitor treatments decreased RNA transcription. Bar, 10 μm. ***$p < 0.0001$, Wilcoxon signed-rank test for control versus DRB ($p < 2.2 \times 10^{-16}$) and for control versus α-AM ($p < 2.2 \times 10^{-16}$) and for control versus ActD ($p < 2.2 \times 10^{-16}$).

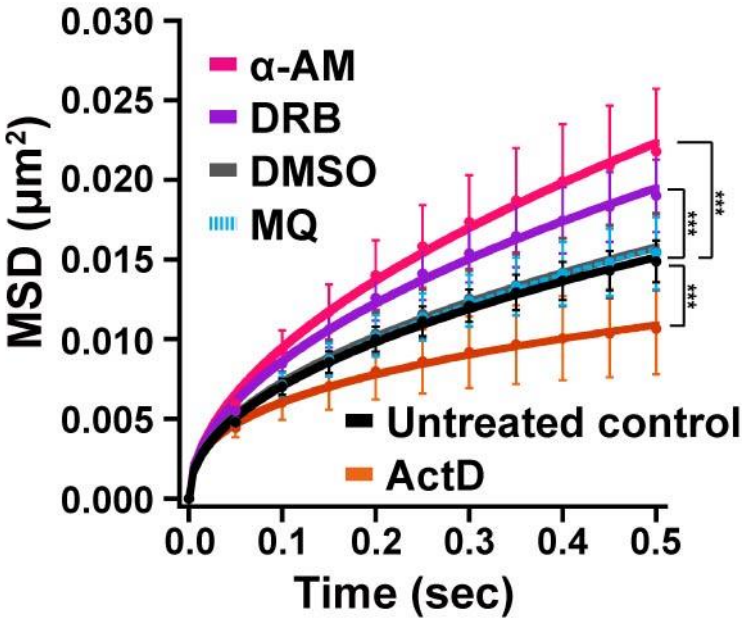

Figure 21. MSD plots of single nucleosomes in RNAPII inhibitor treated RPE-1 cells.

MSD plots (± s.d. among cells) of nucleosomes in the RPE-1 cells treated with RNAPII inhibitors, α-AM (pink), DRB (purple), and ActD (red). The controls are DMSO (gray), MQ (light blue), or untreated (black). For each condition, n = 20 cells. Note that the inhibition of RNAPII increased the chromatin dynamics, except for ActD. ***p<0.0001, Kolmogorov–Smirnov test for untreated control versus DRB ($p = 1.4 \times 10^{-7}$) and for untreated control versus α-AM ($p = 1.1 \times 10^{-8}$) and for untreated control versus ActD ($p = 9.5 \times 10^{-6}$).

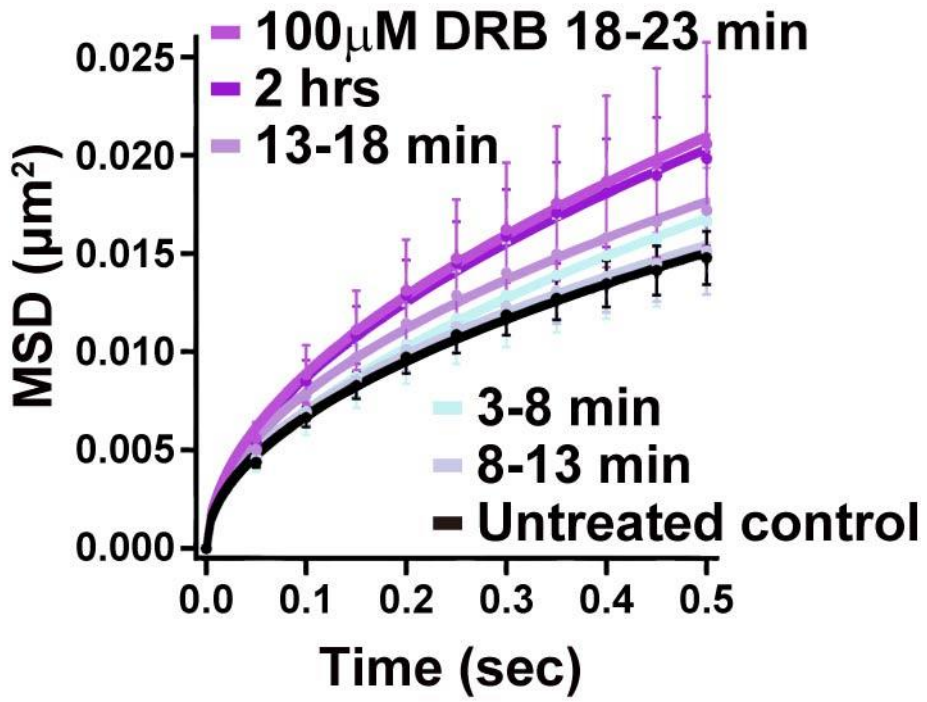

Figure 22. MSD plots of single nucleosomes in DRB treated RPE-1 cells.

MSD plots (± s.d. among cells) of nucleosomes from 0.05 to 0.5 s in RPE-1 cells treated with DRB (colors) for indicated treatment periods, or untreated (control, black). For each condition, n = 3–20 cells. Depending on the treated time with DRB, the chromatin dynamics gradually increased.

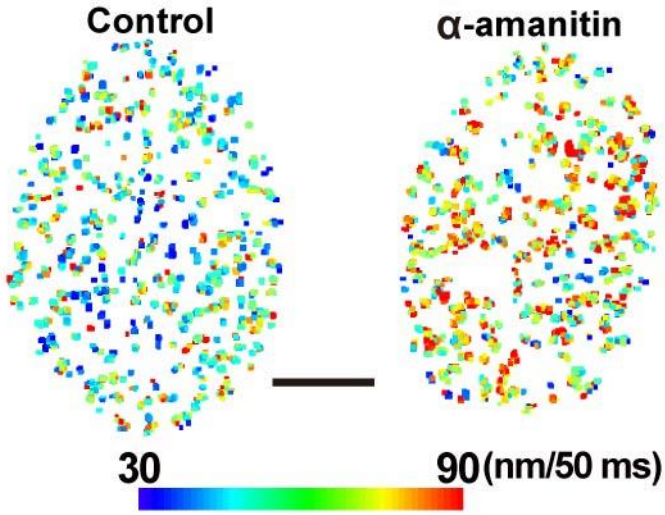

Figure 23. Chromatin heatmaps of the nuclei treated with (right) and without α-amanitin (left).

Larger chromatin movement appears as more “red” (or hot), and smaller movement appears as more “blue” (or cold) pixels. Note that the heatmap of the nucleus with α-AM turned more “red”. Bar, 5 μm.

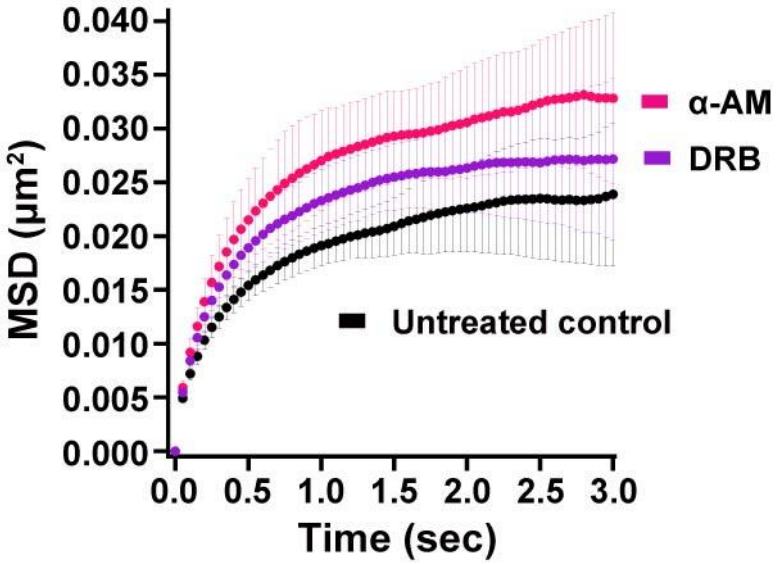

Figure 24. Long term MSD plots of single nucleosomes in transcription inhibitor treated RPE-1 cells. MSD plots (± s.d. among cells) of single nucleosomes in RPE-1 cells treated with RNAPII inhibitor (α-AM, DRB), or without inhibitors (Control) from 0.05 to 3 s. For each sample, n = 20 cells. The inhibitor treatments increased chromatin dynamics with less constraint.

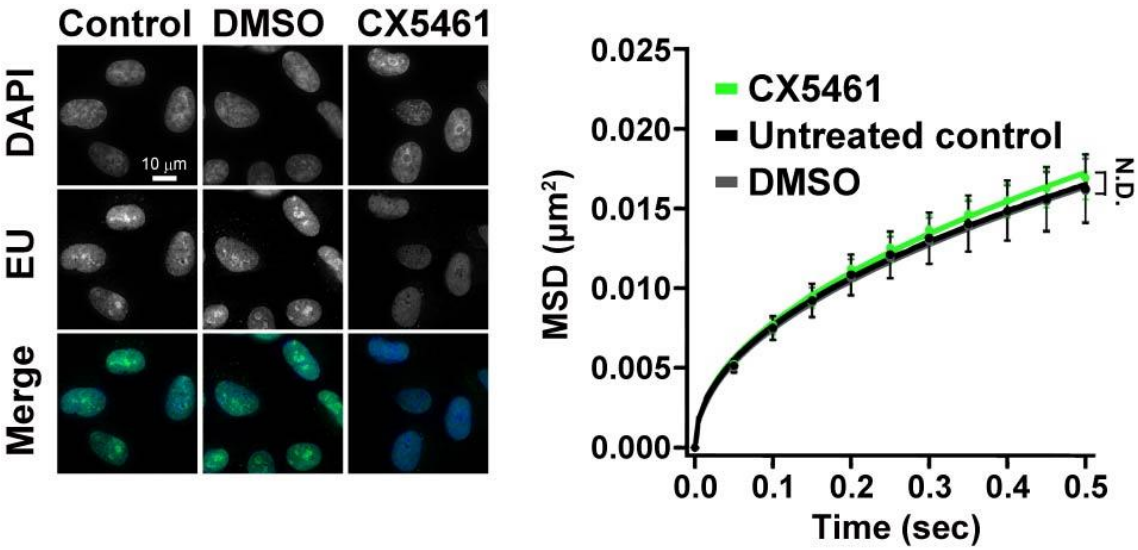

Figure 25. Effect of RNA polymerase I (RNAPI) on nucleosome movement.
(Left) Verification of RNAPI inhibition with CX5461 by EU incorporation. Bar, 10 μm. Signals from nucleoli were decreased in the drug treated cells, indicating reduction of RNAPI activity. (Right) MSD plots (± s.d. among cells) of single nucleosomes in RPE-1 cells treated with RNAPI inhibitor (CX5461, green), solvent (DMSO, gray), or none (Control, black). For each condition, n = 37–39 cells. Note that the effect of RNAPI inhibition on the chromatin dynamics is very small. N.D. means not detected, Kolmogorov–Smirnov test for untreated control versus CX5461 (p = 0.40).

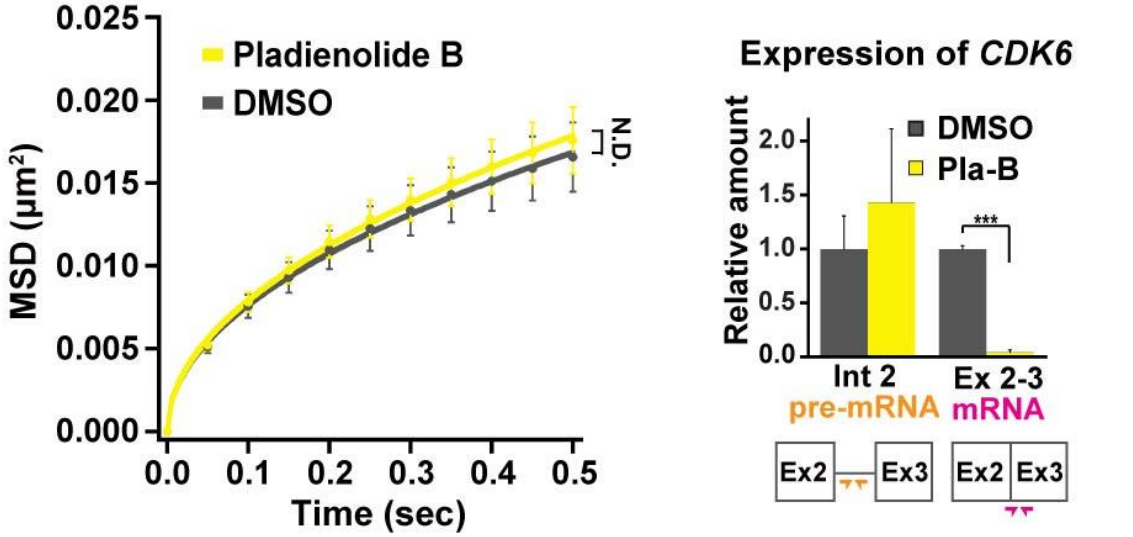

Figure 26. Effect of splicing on nucleosome movement.

(Left) MSD plots (± s.d. among cells) of single nucleosomes in RPE-1 cells treated with splicing inhibitor, Pladienolide B (Pla-B, yellow) or DMSO (gray). For each condition, n = 20 cells. N.D. means not detected, Kolmogorov–Smirnov test (p = 0.34). (Right) Verification of splicing inhibition in RPE-1 cells treated with Pla-B by qRT-PCR. Relative amounts of spliced (Ex 2-3 mRNA) and non-spliced (Int 2 pre-mRNA) CDK6 RNA products in RPE-1 cells treated with Pla-B (yellow) or DMSO (gray) are shown. Schematic representation of primer positions for Ex 2-3 mRNA (pink arrows) and Int 2 pre-mRNA (orange arrows) are also shown at the bottom. Averaged relative amounts of the products were shown with SD (n = 3). ***p < 0.0001, Student's t test ($p = 1.7 \times 10^{-6}$).

Transcriptional inhibition by actinomycin D increased constraints of local chromatin movements

Since the DRB and α-AM treatments described above reduced the amounts of active RNAPIIs on chromatin, I wondered whether stable RNAPII binding to chromatin might induce chromatin stabilization and constraint. To test this possibility, I examined the effect of another inhibitor, actinomycin D (ActD), which induces stalling of active RNAPII on chromatin (Kimura et al., 2002). While ActD treatment reduced global RNA synthesis in the cells (Figure 20), the amounts of both active RNAPII marks in the treated cells were similar or slightly higher than those of the untreated control cells (Figure 17; Figure 18),

suggesting more active RNAPII on the chromatin. In contrast to DRB and α-AM, ActD treatment decreased the chromatin dynamics and induced more constraints (Figure 21). This result supports that active RNAPII complexes on chromatin constrained the local chromatin movements throughout the whole genome.

Transcriptional inhibition didn't affect the physiological environment

As shown by EU incorporation, RNAPII inhibition greatly decreased RNAs production in the nuclei (Figure 20). To exclude the possibility that the transcriptional inhibition might affect the physical chromatin environments and subsequently change chromatin behavior, I further examined two factors, total density (molecular crowding) and free Mg^{2+} concentration in the nuclei. Total densities in the nucleoplasm of α-AM-treated and untreated RPE-1 cells, which were directly measured by OI-DIC microscopy (Imai et al., 2017), were ~130 mg/mL (Figure 27). So total density was not changed after transcriptional inhibition. Regarding Mg^{2+} concentration, although free Mg^{2+} can greatly condense chromatin in the cell by neutralizing electrostatic charge of DNA (Hansen, 2002; Maeshima et al., 2018), I found no significant difference in free Mg^{2+} levels between the treated and untreated cells (Figure 28). These results suggested that transcriptional inhibition didn't affect the physiological environment. Again, the results strengthened the notion that active RNAPII globally restricts the chromatin dynamics.

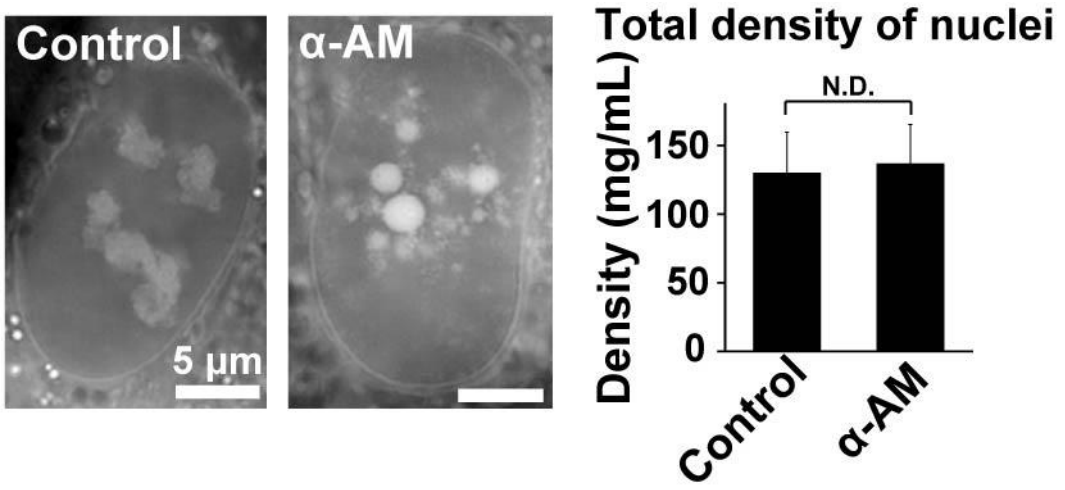

Figure 27. Total densities in the nuclei of living RPE-1 cells treated with or without α-amanitin.
(Left) Total densities in the nuclei of living cells were measured by OI-DIC microscopy (Imai et al., 2017). Typical images of optical pass difference (OPD) map of the cells treated with (right) or without (left) α-AM were shown. (Right) Calculated total densities in the nuclei of RPE-1 cells were depicted as a bar graph with SD. Total nuclear density did not change remarkably with α-AM treatment. For each condition, n = 14–22 cells. Bars, 5 μm. N.D. means not detected, Student's t test (p = 0.50).

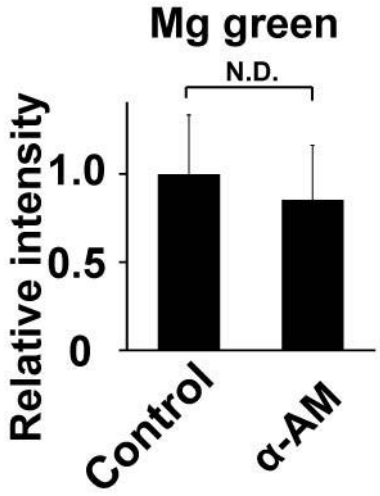

Figure 28. Relative free Mg^{2+} concentrations in RPE-1 cells treated with or without α-amanitin.
Mg^{2+} concentrations in the nuclei of living cells treated with (right) and without (left) α-amanitin were measured by the free Mg^{2+} indicator, Mg-green, and were shown as bar graph with SD. For each condition, n = 33–42 cells. The free Mg^{2+} concentration did not change remarkably with α-AM treatment. N.D. means not detected, Student's t test (p = 0.052).

Transcriptional inhibition didn't affect the chromatin movements at the nuclear periphery

If chromatin movements were globally constrained by transcriptionally active RNAPII, I inferred that the transcriptional inhibition should not affect chromatin dynamics in heterochromatin regions. To test this possibility, I focused on the nuclear bottom surfaces (nuclear periphery) (Shinkai et al., 2016), where condensed lamina-associated domains (LADs) (Van Steensel and Belmont, 2017) are enriched. The regions have fewer active-RNAPII (Figure 19) (Boettiger et al., 2016), and their chromatin is less mobile (Nozaki et al, 2017). To visualize the nuclear surfaces (nuclear periphery), the illumination laser angle in the microscopy was adjusted to efficiently capture a nuclear membrane marker, NUP107-Venus (Maeshima et al., 2010b) (Figure 29). As reported previously (Nozaki et al., 2017), chromatin dynamics on the nuclear surface was lower than those of nuclear interior, which contained more euchromatin regions (Figure 30). α-AM treatment, which showed a great effect in nuclear interior, did not increase the chromatin dynamics on the nuclear surfaces (nuclear periphery) (Figure 30). This finding suggests that RNAPII activity only effects the chromatin dynamics of actively transcribed regions.

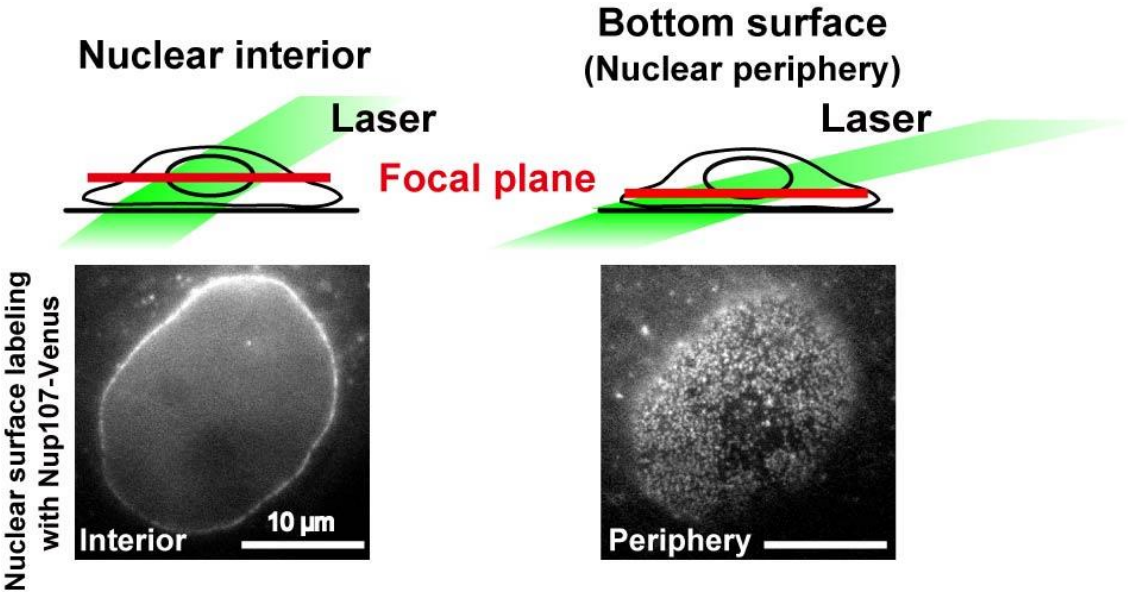

Figure 29. A schematic representation for nuclear interior and nuclear surface (periphery) imaging. A focal plane (red) at nuclear interior (left) or periphery (right) was selected by changing an angle of laser illumination (green). Note that the two different focal planes were precisely verified by nuclear surface labeling with a nuclear pore component NUP107-Venus (Maeshima, 2010b). Almost uniform distributions of NUP107-Venus were observed in the nuclear periphery condition (right), while the nuclear interior condition showed a "rim" of NUP107-Venus (left). Bars, 10 µm.

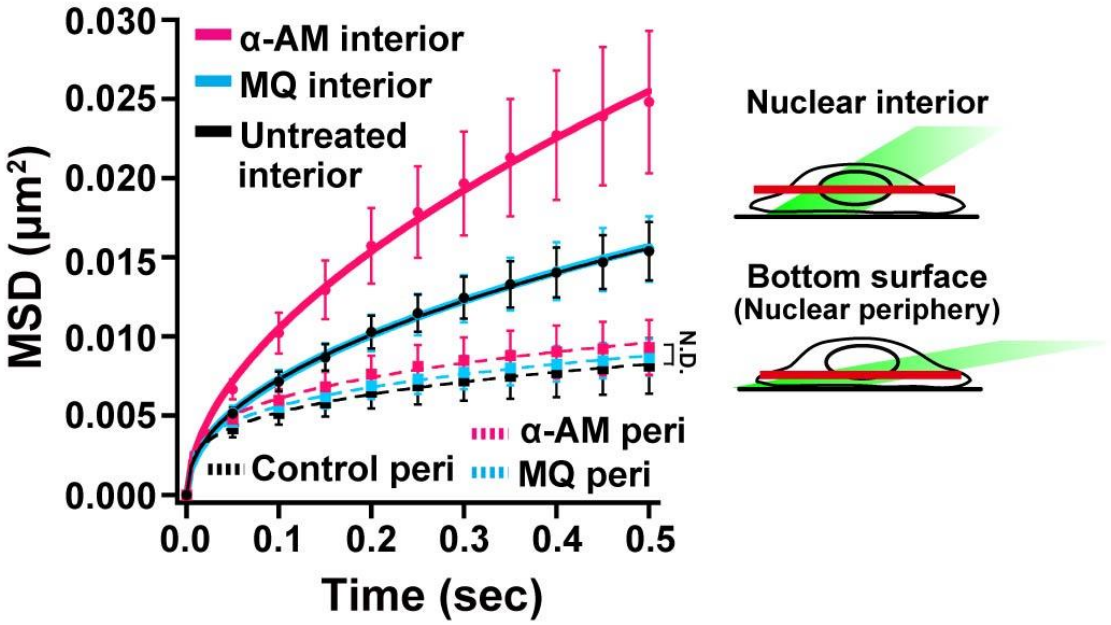

Figure 30. MSD plots of single nucleosomes on the interior and peripheral layers of the RPE-1 cells. (Left) MSD plots (± s.d. among cells) of single nucleosomes on the interior and peripheral (peri) layers of the RPE-1 nuclei treated with RNAPII inhibitor, α-AM (pink), solvent (MQ, light blue), or none (Control, black). For each condition, n = 15 cells. Note that on the nuclear periphery, the chromatin dynamics was not affected by α-AM treatment. N.D. means not detected, Kolmogorov–Smirnov test for control peri versus α-AM peri ($p = 0.075$). (Right) Schematic representation for nuclear interior (upper) and periphery (lower) imaging.

Rapid depletion of RNAPII by auxin-inducible degron (AID) system diminished the chromatin constraints

Inhibitor treatments always have a risk for various indirect effects. For instance, it was reported that long DRB treatment could disrupt nucleolar structure and disperse them through the nuclear interior (Chubb et al., 2002). To validate the involvement of RNAPII in the constraints of chromatin movements more directly, we generated cells that enable us to perform rapid and specific degradation of RPB1, the largest subunit of RNAPII, by an auxin-inducible degron (AID) system (Figure 31) (Natsume et al, 2016; Yesbolatova et al., 2019). I collaborated the establishment of the cell line with Dr. Kanemaki, M.T. (National Institute of Genetics, NIG) and Dr. Natsume, T. (NIG). Using the

CRISPR/Cas9-based genome editing, we introduced a cassette encoding mAID and fluorescent protein, mClover (mAID+mClover) at the initiation site of the endogenous RNAPII gene locus (*POLR2A*) (Figure 32) in human colon adenocarcinoma DLD-1 cells expressing the OsTIR1, which is involved in the induced degradation process (Figure 31) (Natsume et al., 2016; Yesbolatova et al., 2019). The DLD-1 cells that carried a proper insertion of mAID+mClover tag into *POLR2A* gene were selected with hygromycine-resistance and auxin-sensitivity and were further confirmed by PCR to obtain bi-allelic tagged RPB1 (Left, Figure 33). We also verified with immunoblotting that all the fraction of RPB1 protein in clone 1 and 5 was degraded upon auxin addition (Right, Figure 33). For further analysis, H2B-Halo was introduced into clone 5 and we established a cell line stably expressing H2B-Halo in the clone 5 background (Figure 34). In the established cells, RPB1 was depleted within one hour after auxin addition (Figure 34). Similar to the observation when treated with DRB or α-AM, rapid depletion of RPB1 significantly increased the chromatin dynamics (Figure 35), supporting my hypothesis that RNAPII directly constrains chromatin movements.

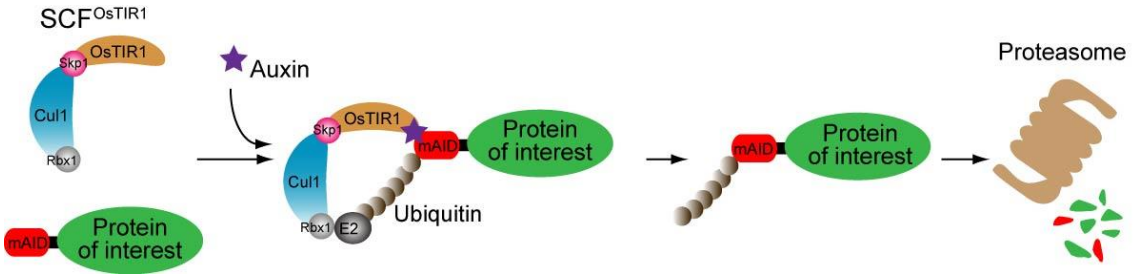

Figure 31. A schematic illustration of the auxin inducible degron (AID) system (Natsume et al., 2016). OsTIR1, which was expressed by addition of Doxycycline (Dox), can form a functional SCF^{OsTIR1} E3 ligase complex with the endogenous components in human cells. In the presence of auxin, a protein of interest fused with mAID is rapidly degraded upon poly-ubiquitylation.

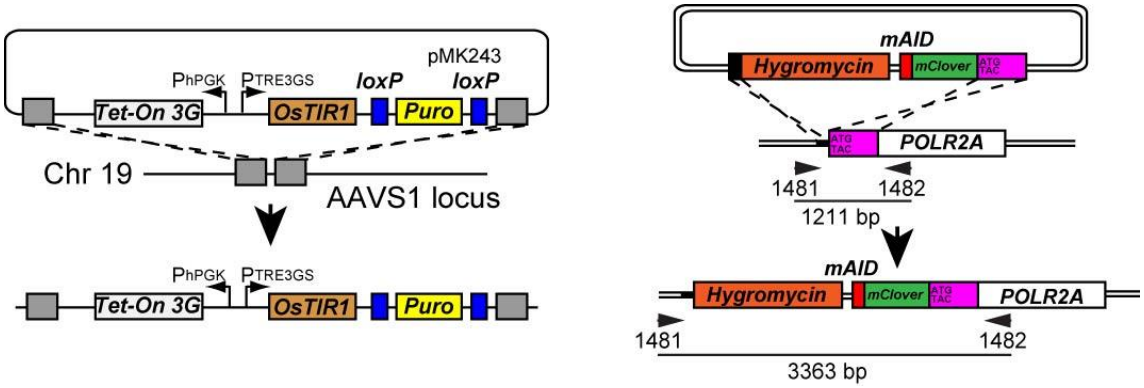

Figure 32. Experimental scheme of how to insert tet-OsTIR1 and mAID tag into DLD-1 cells.
Tet-OsTIR1 was introduced at the safe-harbor AAVS1 locus in human colorectal carcinoma DLD-1 cells (left) and mAID-mClover-RPB1 (mAC-RPB1) cells were generated (right) by a CRISPR/Cas9 genome editing method. Genomic PCR to test the genotype of clones after hygromycin selection was performed. Primer sets and expected PCR products are shown in right panel. After integration at the *POLR2A* gene encoding the largest subunit of RNAPII, RPB1, the PCR primers should give rise to 3.4 kb products in DLD-1 cells.

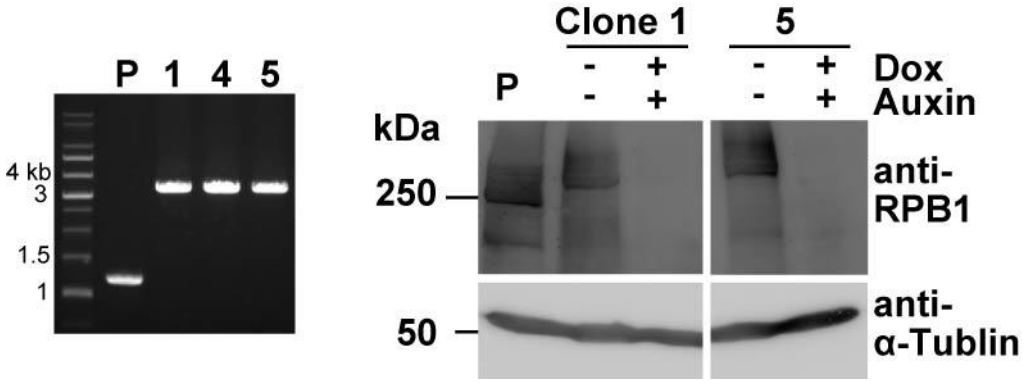

Figure 33. Verification of mAID tag insertion and confirmation of the AID system.
(Left) PCR confirmed that both alleles of *POLR2A* gene were tagged with mAID-mClover. P means parental DLD-1 cell and numbers put on upper of image are cell clone numbers. (Right) RNAPII degradation in DLD-1 cells (clone1, and 5) after the auxin treatment was verified by immunoblotting using an antibody against RPB1 C-Terminal Domain (CTD). α-tubulin was used as a control. Note that the auxin treatment induced RNAPII degradation.

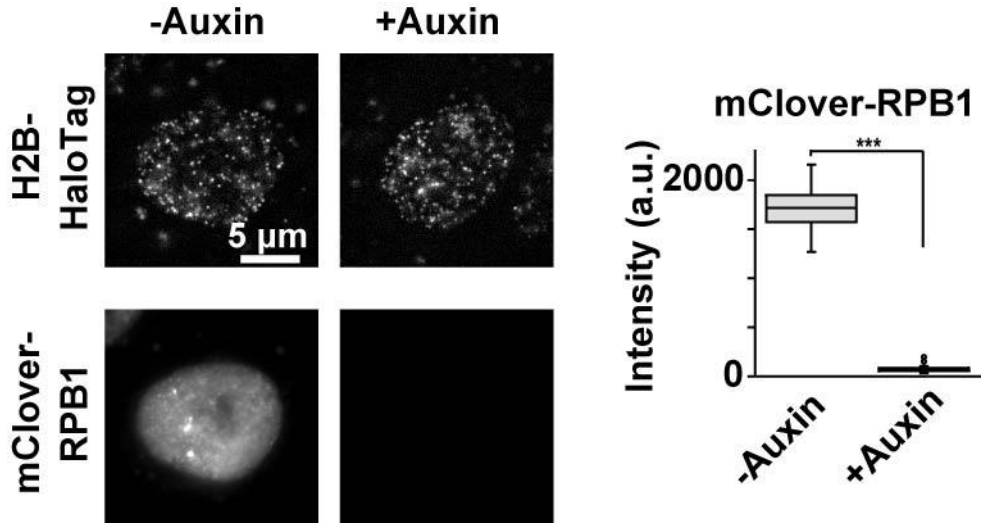

Figure 34. Quantification of Rpb1 degradation after auxin treatment by using fluorescent intensities. (Left) Fluorescent image of H2B-Halo-TMR (upper) and mClover-RPB1 (lower) in living DLD-1 cells before (left) and after treatment with auxin for 1 hr (right). Bar, 5 µm. (Right) The median intensities of mClover-RPB1 are 1717 (n = 30) in untreated control and 61.5 (n = 40) in Auxin treated cells. ***p < 0.0001, Wilcoxon signed-rank test ($p < 2.2 \times 10^{-16}$).

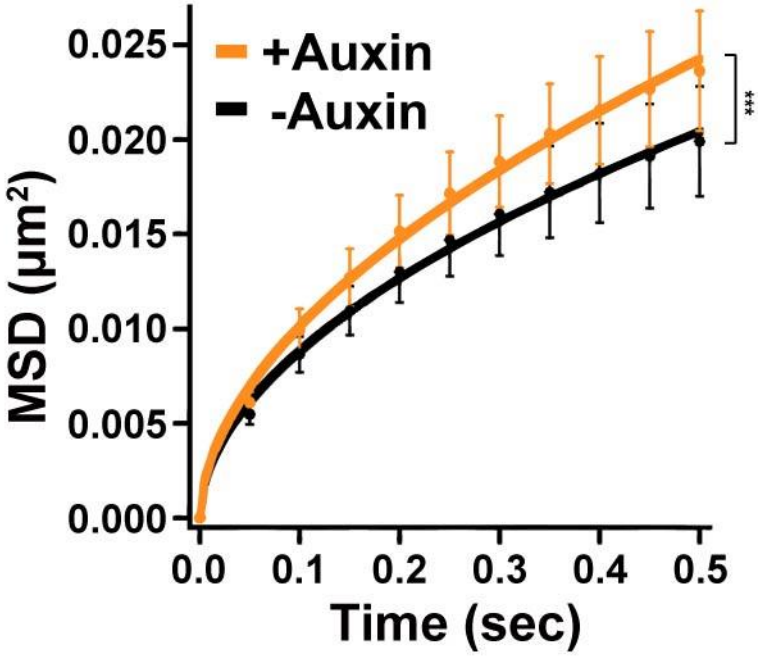

Figure 35. MSD plots of nucleosomes in DLD-1 cells before and after auxin treatment.
MSD plots (± s.d. among cells) of nucleosomes in DLD-1 cells before (-Auxin, black), and 1 hour after auxin induced direct degradation of RNAPII (+Auxin, orange). For each condition, n = 38–39 cells. Note that the prompt degradation of RNAPII increased the chromatin dynamics. ***p < 0.0001, Kolmogorov–Smirnov test ($p = 2.3 \times 10^{-5}$).

Decreased chromatin constraints in the G0 state of RPE-1 cells

To investigate chromatin constraints by active RNAPII in a more physiological state, I induced RPE-1 cells into a transcriptionally less active G0 state by serum removal from the culture medium (Figure 36). G0 entry was confirmed by loss of the proliferation markers Ki67 and Topoisomerase IIα (TopoIIα) in the treated cells (Figure 37 and Figure 38). Serum-starvation for 3 days induced 70 % of the cells into G0, and almost all cells were in G0 after 7 days-starvation. Depending on the starvation periods, the chromatin dynamics increased in the G0 cells (Figure 39). Consistently, signals of two active RNAPII markers (Stasevich et al., 2014) significantly decreased in the G0-cells (Figure 40 and Figure 41). Notably, the decrease in RNAPII-Ser5P, rather than RNAPII-Ser2P, was well correlated with increase in local chromatin dynamics, i.e. decrease in constraints of local chromatin movements (Figure 39; Figure 40; Figure 41). To exclude the possibility that serum starvation changes global chromatin organization to induce an uneven TMR-labeling, which prefers open chromatin regions, H2B-Halo was TMR-labeled prior to serum starvation and observed. The result was consistent with normal labeling method (Figure 42), indicating that serum starvation didn't change global chromatin organization to induce an uneven TMR-labeling.

Figure 36. Experimental scheme of serum starvation and serum stimulation.
Proliferating cells were starved by removing serum from culture medium. Most of the cells entered the G0 phase. The starved cells were then stimulated with serum re-addition to re-enter them into the proliferating state.

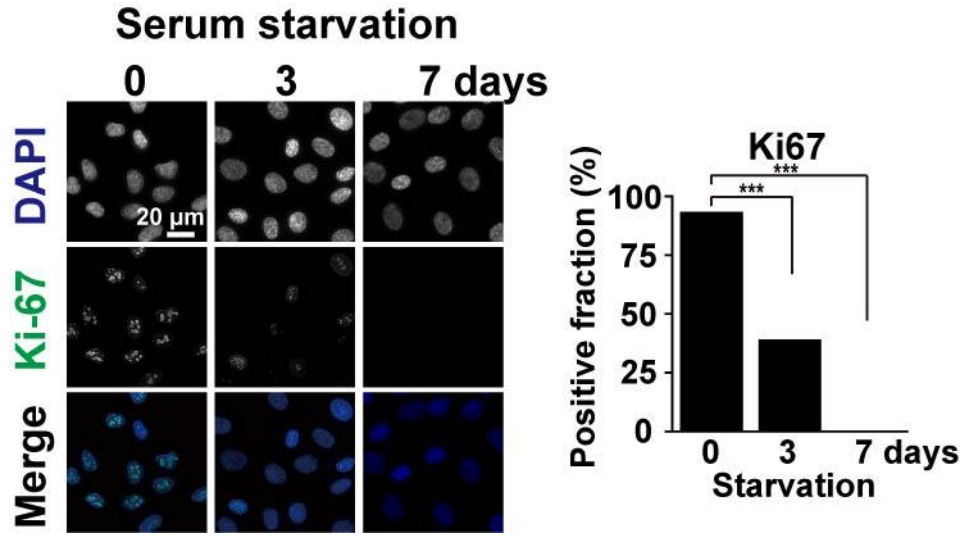

Figure 37. Verification of G0 state of RPE-1 cells by immunostaining with proliferation marker Ki67. The Ki67-positive cells were 93 % in the non-starved cells (0 day) (n = 76; positive = 71, negative = 5), 39 % in the cells starved for 3 days (n = 107; positive = 42, negative = 65), and 0 % in the cells starved for 7 days (n = 111; positive = 0, negative = 111). ***p < 0.0001, Fisher's exact test for 0 day versus 3 days ($p = 5.0 \times 10^{-16}$) and for 0 day versus 7days ($p < 2.2 \times 10^{-16}$). Bar, 20 µm.

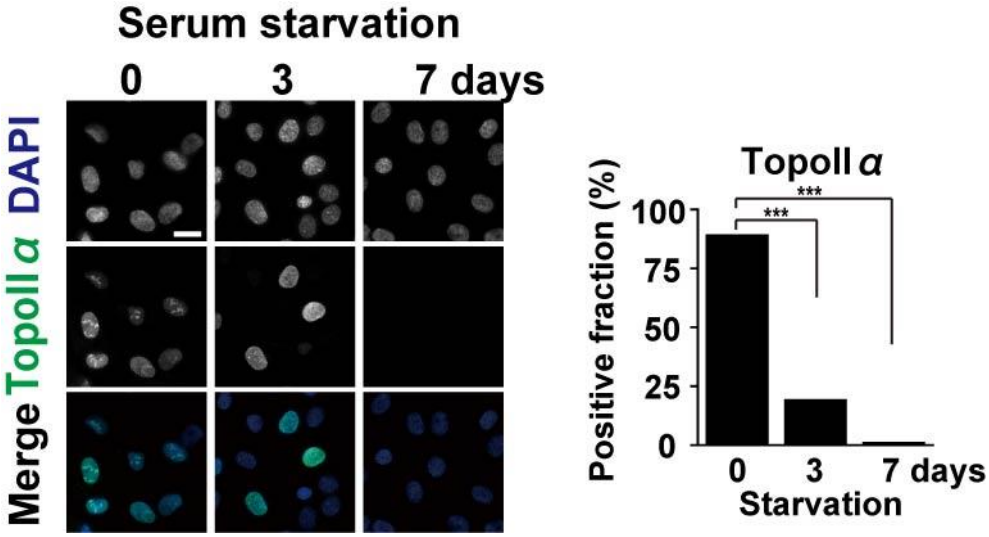

Figure 38. Verification of G0 state of RPE-1 cells by immunostaining with proliferation marker Topoisomerase IIα (TopoIIα).

The TopoIIα-positive cells were 90 % in the non-starved cells (0 day) (n = 67; positive = 60, negative = 7), 20 % in the cells starved for 3 days (n = 97; positive = 19, negative = 78), and 1.5 % in the cells starved for 7 days (n = 67; positive =1, negative = 66). ***p < 0.0001, Fisher's exact test for 0 days versus 3 days ($p < 2.2 \times 10^{-16}$) and for 0 days versus 7days ($p < 2.2 \times 10^{-16}$). Bar, 20 µm.

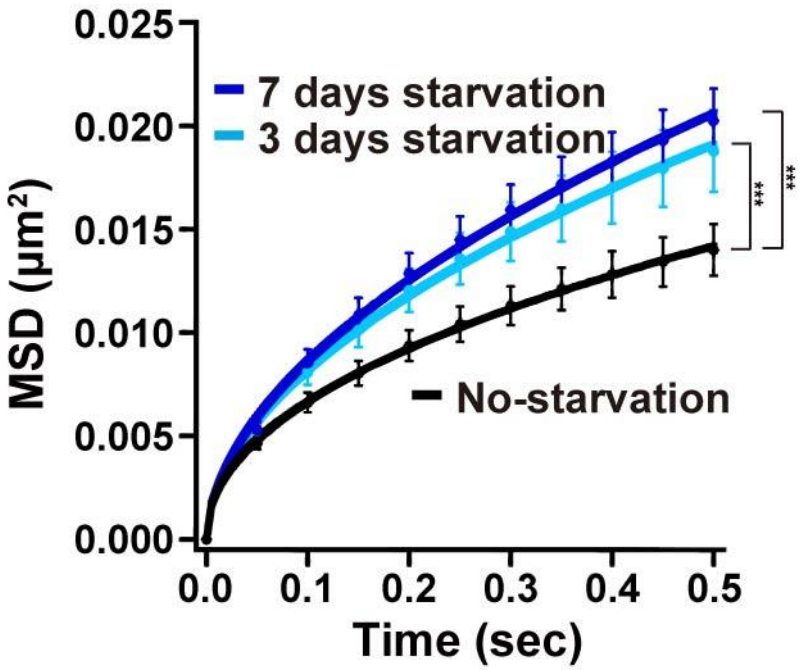

Figure 39. MSD plots of nucleosomes after serum starvation in RPE-1 cells.

MSD plots (± s.d. among cells) of nucleosomes in RPE-1 cells (black), and with the serum starvation for 3 days (light blue) or 7 days (dark blue). For each condition, n = 20 cells. Note that the chromatin dynamics increased depending on the serum starvation period. ***$p < 0.0001$, Kolmogorov–Smirnov test for No-starvation versus 3 days starvation ($p = 1.1 \times 10^{-8}$) and for No-starvation versus 7 days starvation ($p = 1.5 \times 10^{-11}$).

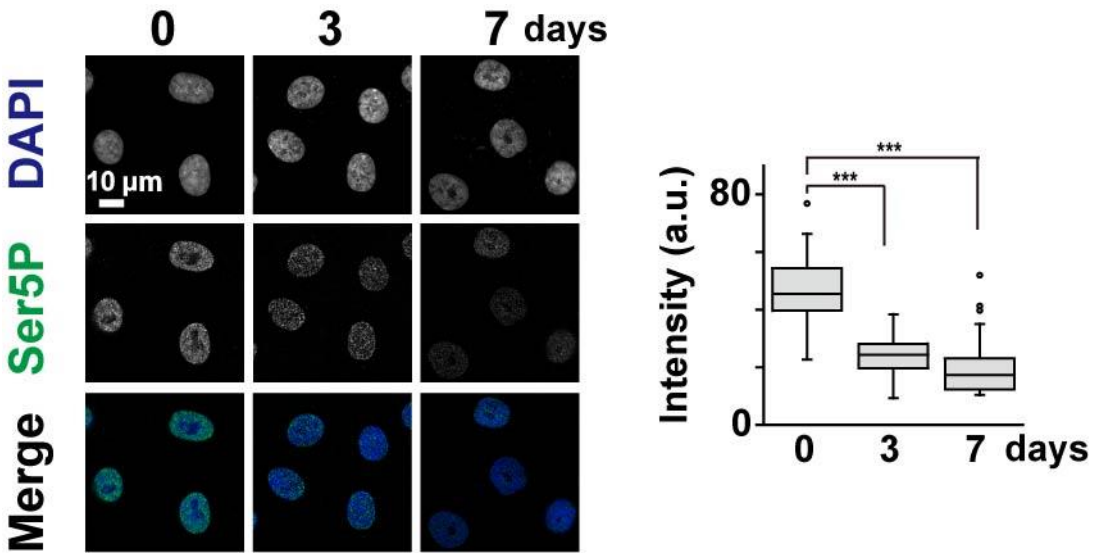

Figure 40. Verification of RNAPII activity after serum starvation by using RNAPII-Ser5P antibody. (Left) RNAPII activity of RPE-1 cells without (0 day) or with the serum starvation for 3 days and 7 days were investigated by immunostaining of Ser5P of the RPB1 CTD in RNAPII. (Right) Quantifications of RNAPII-Ser5P signal intensity are shown as box plots. The median intensities of Ser5P are 45.5 (n = 38) in 0 day starvation, 24.4 (n = 47) in 3 days, and 17.3 (n = 42) in 7 days. RNAPII activity decreased after the serum starvation. Bar, 10 µm. Wilcoxon signed-rank test for 0 days versus 3 days ($p < 2.2 \times 10^{-16}$) and for 0 days versus 7 days ($p < 2.2 \times 10^{-16}$).

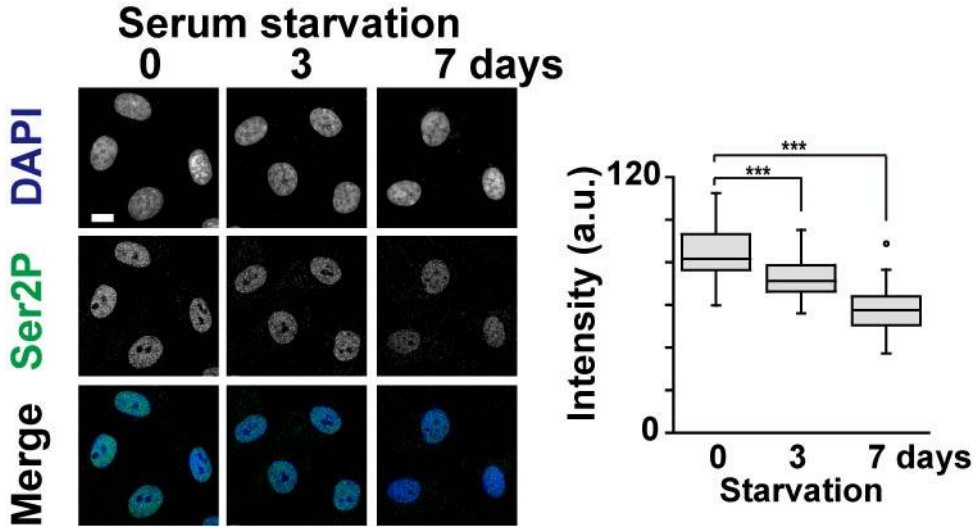

Figure 41. Verification of RNAPII activity after serum starvation by using RNAPII-Ser2P antibody. (Left) RNAPII activity of RPE-1 cells without (0 day) or with the serum starvation for 3 days and 7 days were investigated by immunostaining of Ser2P of the RPB1 CTD in RNAPII. (Right) Quantifications of RNAPII Ser2P signal intensity are shown as box plots. The median intensities of Ser2P are 81.7 (n = 41) in 0 day starvation, 71.3 (n = 42) in 3 days starvation, and 57.6 (n = 39) in 7 days starvation. RNAPII activity decreased after the serum starvation. Bar, 10 μm. ***$p < 0.0001$, Wilcoxon signed-rank test for 0 days versus 3 days ($p = 9.5 \times 10^{-12}$) and for 0 days versus 7 days ($p < 2.2 \times 10^{-16}$).

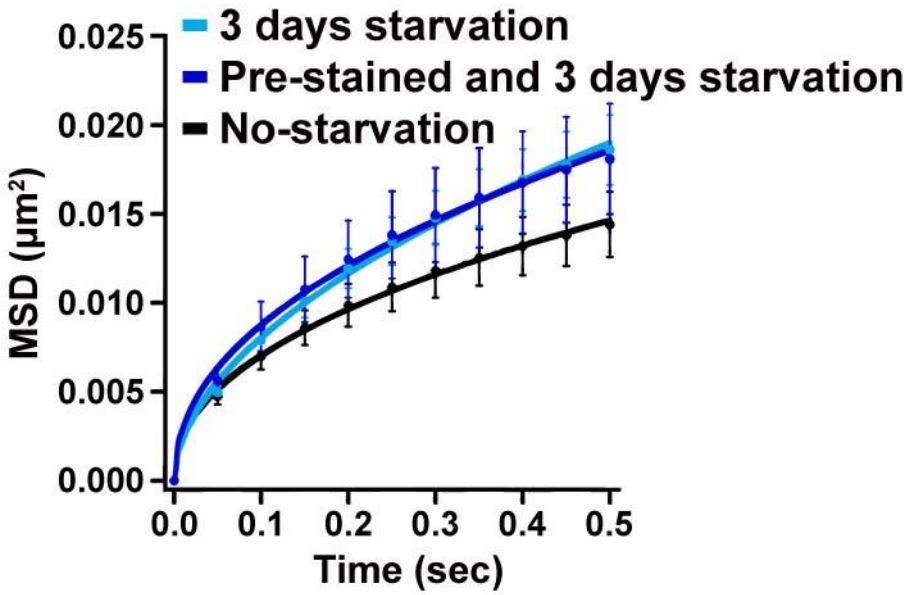

Figure 42. MSD plots of nucleosomes which were pre-stained with TMR before starvation.
MSD plots (± s.d. among cells) of nucleosomes in RPE-1 cells without starvation (black) and with 3 days serum starvation (light blue), and also nucleosomes TMR-stained before starvation and with the 3 days starvation (pre-stained, dark blue) to exclude the possibility that the starvation-induced chromatin change might affect TMR-labeling. For each condition, n = 14–27 cells. Note that the chromatin dynamics were unchanged regardless of when the nucleosomes were labeled with TMR dye.

Serum re-addition restored the chromatin constraints

I then examined an effect of serum re-addition on the G0-cells. One day after serum restoration, the cells became Ki67-positive, which is similar to that of normal proliferating cells (Figure 43), suggesting that serum starved RPE-1 cells stayed at quiescent G0 state (Cheung and Rando, 2013). And the serum re-added cells suppressed chromatin movements (Figure 44), which is similar to that of normal proliferating cells. Concurring with this dynamics decrease, the two active RNAPII marks were restored (Figure 45 and Figure 46). Taken together, decrease in transcription in the quiescent G0-cells released constraints of chromatin movements.

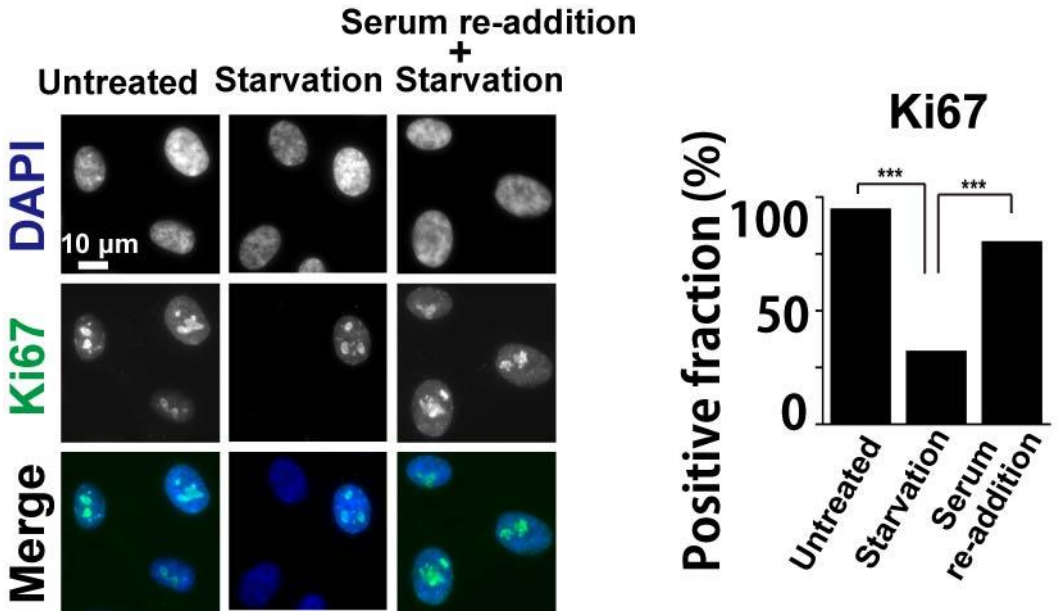

Figure 43. Verification of proliferation state re-entered from G0 phase by immunostaining of Ki67. Positive fractions of Ki67 signal are shown as bar graph. The values are 95 % (n = 101 cells; positive = 96 cells, negative = 5 cells) in the cells without starvation, 32 % (n = 111 cells; positive = 36 cells, negative = 75 cells) in those with 3 days starvation, and 81 % (n = 67 cells; positive = 54 cells, negative = 13 cells) in the cells with serum re-addition after 3 days starvation. ***$p < 0.0001$, Fisher's exact test for untreated versus starvation ($p < 2.2 \times 10^{-16}$) and for starvation versus serum re-addition ($p = 2.9 \times 10^{-10}$). The Ki67 positive cells were restored to almost same level as untreated proliferating cells, indicating that serum starved RPE-1 cells stayed at quiescent state.

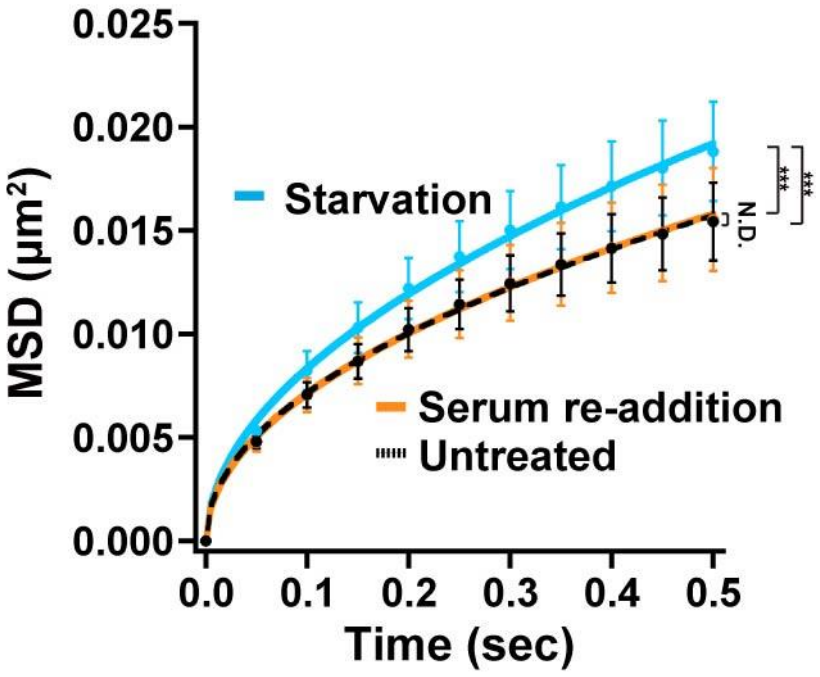

Figure 44. MSD plots of nucleosomes in RPE-1 cells after serum re-addition.

MSD plots (± s.d. among cells) of nucleosomes in RPE-1 cells without (black) or with serum starvation for 3 days (light blue), and 1 day after serum re-addition (orange). For each condition, n = 39–40 cells. The up-regulated chromatin dynamics was restored to the untreated level upon the serum re-addition. N.D. means not detected, ***$p < 0.0001$, Kolmogorov–Smirnov test for untreated versus 3 days starvation ($p = 3.2 \times 10^{-7}$) and for 3 days starvation versus serum re-addition ($p = 4.8 \times 10^{-6}$) and untreated versus serum re-addition ($p = 0.934$).

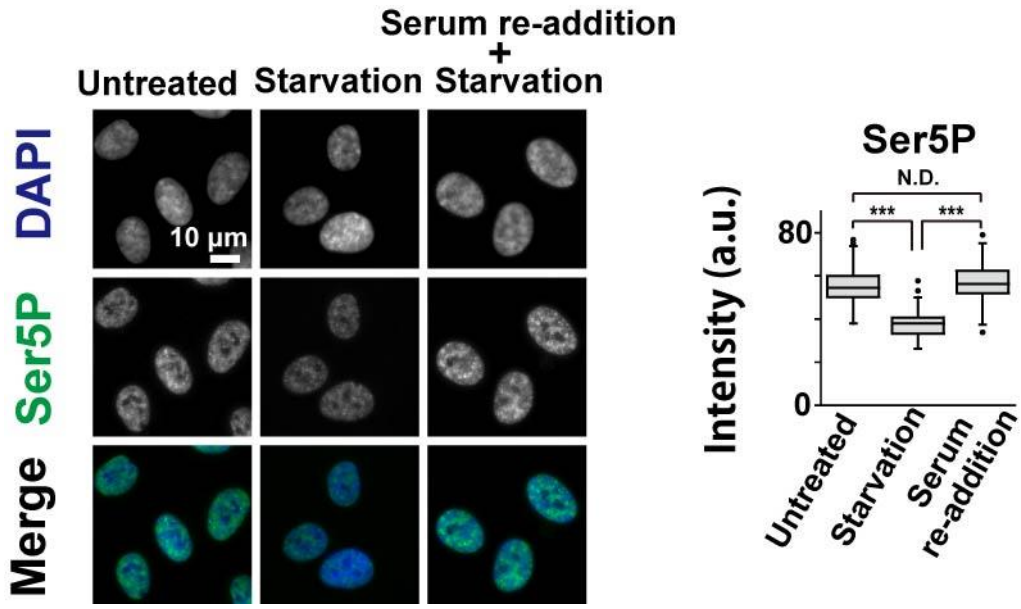

Figure 45. Verification of RNAPII activity after serum re-addition by using RNAPII-Ser5P antibody. RNAPII activity observed by immunostaining in the RPE-1 cells without (untreated control), with serum starvation for 3 days, or with the re-addition of serum. Quantifications of RNAPII-Ser5P signal intensity are shown as box plots. The median intensities of Ser5P are 54.5 (n = 101) in untreated control, 38.0 (n = 103) 3days starvation, and 56.3 (n = 79) in re-addition. Note that RNAPII activity decreased in the quiescent G0 phase and was restored with the serum re-addition. Bar, 10 μm. N.D. means not detected, ***$p < 0.0001$, Wilcoxon signed-rank test for untreated versus starvation ($p < 2.2 \times 10^{-16}$) and for starvation versus serum re-addition ($p < 2.2 \times 10^{-16}$) and for untreated versus serum re-addition ($p = 0.1981$).

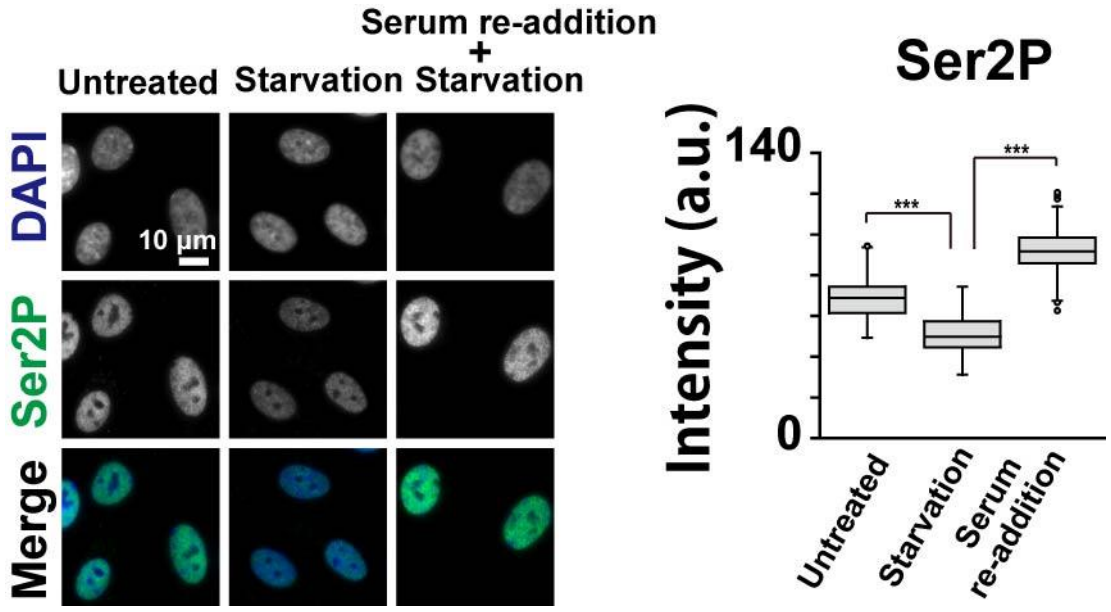

Figure 46. Verification of RNAPII activity after serum re-addition by using RNAPII-Ser2P antibody. RNAPII activity observed by immunostaining in the RPE-1 cells without (untreated control), with serum starvation for 3 days, or with the re-addition of serum. Quantifications of RNAPII Ser2P signal intensity is shown as box plots. The median intensities of Ser2P are 68.7 (n = 105) in the cells without starvation, 49.8 (n = 96) in 3 days starvation, and 91.7 (n = 67) in serum re-addition. Note that RNAPII-Ser2P decreased in the quiescent G0 phase and was restored upon the re-entering the cell cycle after the serum re-addition. ***$p < 0.0001$, Wilcoxon signed-rank test for untreated versus starvation ($p < 2.2 \times 10^{-16}$) and for starvation versus serum re-addition ($p < 2.2 \times 10^{-16}$).

Loose genome chromatin domain network via active RNA polymerase II

What is the underling molecular mechanism for globally constraining chromatin motion? Our previous study showed that the nucleosomes within the domain seem to move coherently in living cells (Nozaki et al., 2017). Based on the available and obtained data, I hypothesize that transcription complex/clusters including RNAPII-Ser5P weakly connect multiple chromatin domains for a loose spatial genome chromatin network (Figure 47) and that thereby chromatin is globally stabilized or constrained by the loose network (Figure 47). Recent studies have shown that active RNAPII, Mediator, and other transcription factors form transient and dynamic clusters (Cho et al., 2016; Cho et al.,

2018; Chong et al., 2018; Cisse et al., 2013; Sabari et al., 2018). Other studies reported that P-TEFb complex consisting of Cyclin T1 (CYCT1) and CDK9 kinase, which interact with RNAPII and phosphorylates its CTD, form a number of stable and dynamic clusters in living cells (Ghamari et al., 2013; Lu et al., 2018). Considering that CDK9 and RNAPII-Ser5P co-occupy thousands of promoter-proximal region of transcribed genes in the reported genomics data (Ghamari et al., 2013), the P-TEFb clusters, including possible other transcription factors, can provide the multiple weak interactions between P-TEFb, RNAPII-Ser5P, and transcribed DNA regions (Cho et al., 2018; Chong et al., 2018; Ghamari et al., 2013; Sabari et al., 2018) (Figure 47). In this context, the P-TEFb clusters and RNAPII-Ser5P can work as “hubs” and “glues” for the multiple weak interactions in the network, respectively (Figure 47). The chromatin domain movements, which seem to be driven essentially by Brownian motion in living cells (Nozaki et al., 2017), are thus globally constrained by the loose network (Figure 47). Consistent with this hypothesis, knockdown (KD) of CDK9 kinase by siRNA upregulated chromatin movements upon reduction of CDK9 protein levels (Figure 48 and Figure 49). Furthermore, DRB treatment, which is also known as the inhibitor of P-TEFb (Bensaude, 2011), had a similar result (Figure 21 and Figure 22). These data suggested that perturbations of P-TEFb clusters lead to loss of the chromatin network hubs and subsequent increase in chromatin movements.

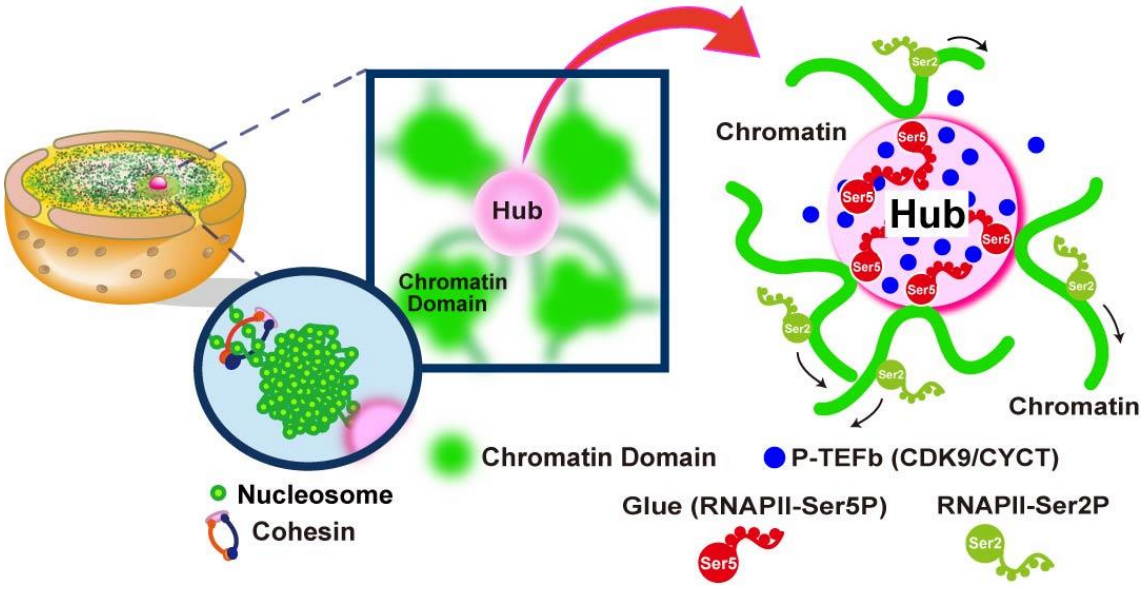

Figure 47. A model for the formation of a loose spatial genome chromatin network via RNAPII-Ser5P. P-TEFb complex (blue sphere) consisting of Cyclin T (CYCT) and CDK9 kinase, which interacts with RNAPII, form a number of stable and dynamic clusters/foci in living cells (pink spheres in the center and right panels) (Ghamari et al., 2013). (Center) The P-TEFb cluster (pink sphere) can work as a "hub" to weakly connect multiple chromatin domains (green spheres) for a loose spatial genome network. (Right) RNAPII-Ser5P (red) can function in the hub as "glue" for the weak interactions between P-TEFb (blue spheres) and transcribed DNA regions (green lines) (Ghamari et al., 2013). Since, after phosphorylation of RNAPII by P-TEFb, RNAPII-Ser2P seems to leave the hubs (P-TEFb clusters) for elongation and processing process (Ghamari et al., 2013), it is unlikely to function as the glue for the connections (Right). Note that this scheme is highly simplified. Besides the P-TEFb clusters, other clusters including transcription factors, Mediator and active RNAPII (Cho et al., 2018; Sabari et al, 2018; Chong et al, 2018) might also work as hubs.

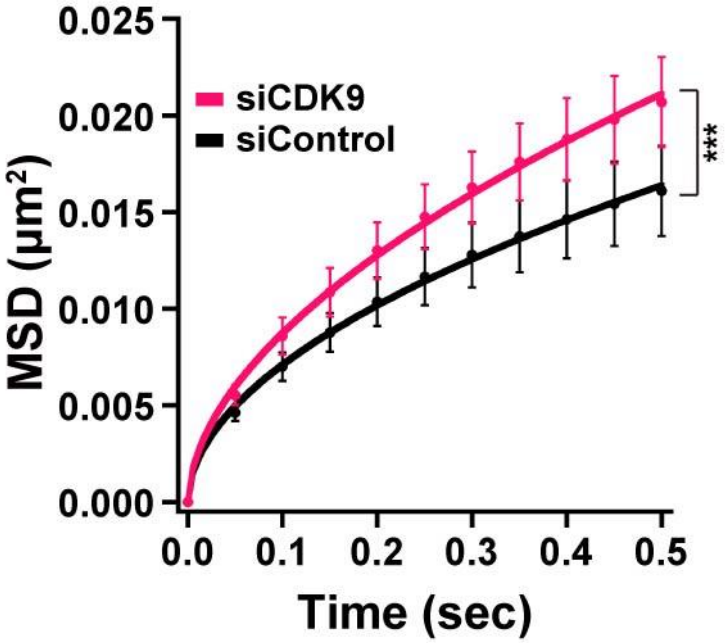

Figure 48. MSD plots of nucleosomes in CDK9-knockdown RPE-1 cells.

MSD plots (± s.d. among cells) of nucleosomes in CDK9-knockdown (KD) RPE-1 cells (siCDK9, pink), and control (siControl, black). For each condition, n = 20 cells. Note that the KD of CDK9 increased the chromatin dynamics. ***$p < 0.0001$, Kolmogorov–Smirnov test ($p = 1.3 \times 10^{-6}$).

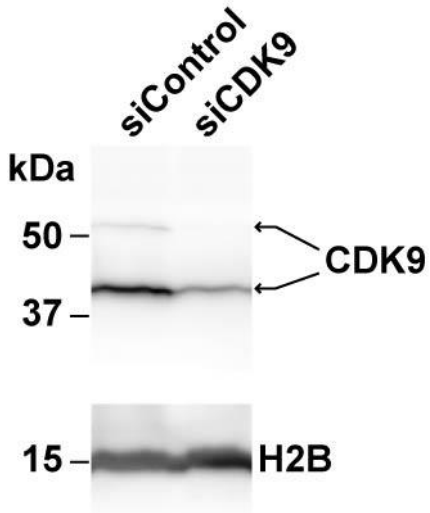

Figure 49. Verification of CDK9 knockdown.

CDK9 reduction in RPE-1 cells after RNA interference was verified by immunoblotting. H2B protein was used as a loading control.

Discussion

Using single nucleosome imaging, I investigated genome-wide chromatin dynamics in a whole nucleus of living cells, and demonstrated the constraints on chromatin movements via active RNAPII (Figure 47). Similar constraints by active RNAPII were observed in more physiological contexts of the cell, such as quiescent G0-state with serum starvation (Figure 39 and Figure 44). This was an unexpected finding, but seems to be general response in the cells. On the other hand, behavior of the chromatin around nuclear periphery is insensitive to a transcriptional suppression (Figure 30). This may not be so surprising because these regions are enriched with LADs tethered to the inner nuclear membrane structures (Lemaitre and Bickmore, 2015) and have few active-RNAPII (Figure 19).

My finding demonstrated that RNAPII is directly involved in constraining genome chromatin and also suggests the existence of a loose chromatin domain network in a whole nucleus via RNAPII-Ser5P (Figure 47). While the classical transcription factory model (Buckley et al., 2014; Feuerborn and Cook, 2015) is consistent with my finding, recent reports showed that RNAPII and other factors form transient and dynamic clusters, but not static ones, prior to the transcription elongation process (Cho et al., 2016; Cho et al, 2018; Chong et al., 2018; Cisse et al., 2013). This transient clustering of RNAPII and other factors might regulate the amount of synthesized RNA output (Cho et al., 2016; Cho et al, 2018). Other studies reported that P-TEFb complexes form a number of stable and dynamic clusters/foci in living cells (Ghamari et al., 2013; Lu et al., 2018) and then recruit RNAPII and phosphorylates its CTD for a trigger of the transcription elongation process (Figure 47). Recent studies also suggested that some of these clusters are liquid like-

compartments (Cho et al., 2018; Chong et al., 2018; Lu et al., 2018; Sabari et al., 2018). Within the clusters/droplets of RNAPII and other transcription factors might be concentrated together to promote functional interactions between them, leading to highly efficient Ser2 phosphorylation of the CTD and subsequent entry into elongation (Figure 47) (Cho et al., 2018; Chong et al., 2018; Lu et al., 2018; Sabari et al., 2018). Furthermore, the hub function of the clusters/droplets might mediate chromatin domain contacts (Figure 47) and further intra-chromosomal and inter-chromosomal interactions for global control of gene transcription.

In my model (Figure 47), perturbations of P-TEFb clusters (hub) by DRB (Figure 21) or CDK9 KD (Figure 48), or removal of RNAPII (glue) (Figures 21 and Figure 35) would lose the glues for connections between the hubs and chromatin domains, leading to decrease in global chromatin constraints. Furthermore, the amount of RNAPII-Ser5P is well correlated with constraints of chromatin movements (Figure 17; Figure 21; Figure 39; Figure 40): the less RNAPII-Ser5P is, the less chromatin constrains induce. On the other hand, RNAPII-Ser2P seems to leave the hubs for elongation and RNA processing process (Figure 16 and Figure 47) (Ghamari et al., 2013) and is unlikely to function as the glue for the connections. This is in agreement with my observation that inhibition of the splicing complex, which is supposedly associated with RNAPII-Ser2P complex going along the template DNA, did not affect the local chromatin behavior (Figure 26). My model (Figure 47) also implies that if I just focus on transcriptional regulatory elements, to which the hubs and RNAPII-Ser5P bind (Ghamari et al., 2013), during transcription elongation the regulatory elements leave the hubs and their movements should increase. Notably, using a very elegant fluorescent labeling of transcriptional regulatory elements,

Gu et al. demonstrated that their movements indeed increased upon transcription activation (Gu et al., 2018).

Interestingly our previous super resolution imaging showed that transcriptional inhibition did not alter the chromatin domain/cluster organization while the domain formation was governed by both local nucleosome-nucleosome interactions and by nucleosome fiber looping through cohesin (round inset in Figure 47) (Nozaki et al., 2017). This suggested that active RNAPII is involved in connecting chromatin domains, but not in chromatin domain formation (Center, Figure 47). Since nucleosomes in the domains seem to move coherently in living cells (Nozaki et al., 2017), constraining domain movements by active RNAPII can also explain how active RNAPII can globally stabilize genome chromatin even though the chromatin regions being transcribed by RNAPII are quite limited in the genome (Djebali et al., 2012). Consistent with our finding by super resolution imaging (Nozaki et al., 2017), a recent study by Hi-C showed that transcriptional inhibition had no appreciable effect on chromatin loop domain formation (Vian et al., 2018). The P-TEFb cluster and possible other clusters recently reported (Cho et al., 2018; Chong et al., 2018; Sabari et al., 2018) might also play an important role in various intra-chromosomal and inter-chromosomal domain contacts that the Hi-C contact probability maps have revealed. It would be interesting to pursue by Hi-C the effect of transcriptional inhibition on higher order organization beyond the domains, such as chromatin compartments.

While the present study revealed the existence of the loose spatial genome network glued by active RNAPII (Figure 47), I inferred that the up-regulation of the local chromatin fluctuation in the transcriptionally suppressive cells has a physiological relevance. Since

our previous Monte Carlo simulation study suggested that increase in local chromatin dynamics can facilitate chromatin accessibility of transcription factors and other proteins (Hihara et al., 2012), in the transcriptionally suppressive cells or quiescent G0 cells the chromatin becomes more dynamic and may be in a high competency state for rapid and efficient recruitment of transcription factors to turn on certain genes in response to extracellular signals.

Materials and Methods

Plasmid construction

pPB-CAG-H2B-PA-mCherry plasmid was constructed based on pPB-CAG-IB (Sanger Institute (MTA)) vector and pEF1α-H2B-PA-mCherry vector (Nozaki et al., 2017). From pEF1α-H2B-PA-mCherry, cDNA of H2B-PA-mCherry was amplified with the addition of *Xho*I site to the both ends by using the following primer pairs:

5'- CCGCTCGAGATGCCAGAGCCAGCGAAGTC -3'

5'- CCGCTCGAGTTACTTGTACAGCTCGTCCATGCCG-3'

The amplified H2B-PA-mCherry was inserted into pPB-CAG-IB digested with *Xho*I.

To construct pPB-CAG-H2B-HaloTag plasmid, cDNA of PA-mCherry in pPB-CAG-H2B-PA-mCherry vector was replaced with HaloTag. The HaloTag fragment was amplified from pFC14A-HaloTag® CMV Flexi vector (Promega) with the addition of *Bam*HI and *Hpa*I sites to the ends in three steps by using the following primer pairs:

5'-TGGAGGTGGAGGCTCTGGTGGCGGTTCCGAAATCGGTACTGG-3'

5'-CCAGTTAACTTAACCGGAAATCTCCAGAG-3'

and

5'-TGGTTCAGGCGGAGGTGGAAGTGGAGGTGGAGGCTCTGGTGG-3'

5'-CCAGTTAACTTAACCGGAAATCTCCAGAG-3'

and

5'- CGCGGATCCATCTGGTGGAGGTGGTTCAGGCGGAGGTGGAAG-3'

5'- CCAGTTAACTTAACCGGAAATCTCCAGAG-3'

pPB-CAG-H2B-PA-mCherry vector and the amplified HaloTag fragment were digested with *Bam*HI and *Hpa*I, and then ligated.

To construct parental DLD-1 cells expressing OsTIR1, a donor plasmid containing tet-OsTIR1 was integrated at the safe harbor AAVS1 locus by using CRISPR–Cas9-based gene editing (Natsume et al., 2016; Yesbolatova et al., 2019). This parental DLD-1 cell line was further transfected with a CRISPR–Cas9 plasmid (based on pX330; Addgene 24430) and a donor, which contains a Hygro-P2A-mAID-mClover cassette flanked with 500 bp homology arms, to insert the cassette next to the 1st methionine codon (Figure 32). The CRISPR–Cas9 is designed to target 5'-GCCACCCCCGTGCATGG/CGGagg-3' in the first exon of the *POLR2A* gene.

Cell culture

RPE-1 and HeLaS3 cells were cultured at 37°C in 5 % CO_2 in Dulbecco's modified Eagle's medium (DMEM) supplemented with 10 % fetal bovine serum (FBS) (Hihara et al., 2012; Nozaki et al., 2017). DLD-1 cells were cultured at 37°C in 5 % CO_2 in RPMI-1640 medium supplemented with 10% FBS. For serum starvation, RPE-1 cells were cultured in DMEM supplemented with 1 % bovine serum albumin (BSA) for 3-7 days. For single nucleosome imaging, cells were cultured on poly-L-lysine coated glass based dishes using phenol red free DMEM supplemented with 10 % FBS or 1 % BSA.

Establishment of cell lines

To establish RPE-1 cell lines stably expressing H2B-Halo or H2B-PA-mCherry, the transposon system was used. The constructed plasmid pPB-CAG-IB-H2B-HaloTag or pPB-PGKneo-EF1-H2B-PA-mCherry (Nozaki et al., 2017) was co-transfected with pCMV-hyPBase (provided from Sanger Institute) to RPE-1 cells with the Effectene transfection reagent kit (QIAGEN). Transfected cells were then selected with 10 μg/mL blasticidin S (Wako) for pPB-CAG-IB-H2B-HaloTag or 600 μg/mL G418 for H2B-PA-

mCherry.

To establish DLD-1 cell line, initially a Tet-OsTIR1 construct (pMK243) was introduced at the safe harbor AAVS1 locus (Natsume et al., 2016; Yesbolatova et al., 2019). Subsequently, I transfected a CRISPR-Cas9 plasmid targeting the N-terminus coding region of the RPB1 gene (GCCACCCCCGTGCATGGCGG) with a donor harboring a Hygro-P2A-mAID-mClover cassette with 500 bp homology arms. After selection with 200 μg/mL hygromcin (Invitrogen), colonies were isolated and confirmed the proper insertion by performing genomic PCR and western blotting. The genomic PCR was performed using following primers:

5'-CTTCTCTCCCTGTCACTTCAAAAGG-3'

5'-CTATTCGAGACAAATGCCATTAAC-3'

The subsequent processes to add H2B-Halotag were done following the case with RPE-1.

Nup107-Venus expressed HeLa cells were described previously (Maeshima et al, 2010b).

Biochemical fractionation of nuclei from cells expressing H2B-Halotag

Nuclei were isolated from RPE-1 cells expressing H2B-Halotag as described previously (Maeshima et al., 2016; Nozaki et al., 2017). Briefly, collected cells were suspended in nuclei isolation buffer (3.75 mM Tris-HCl [pH 7.5], 20 mM KCl, 0.5 mM EDTA, 0.05 mM spermine, 0.125 mM spermidine, 1 mg/ml Aprotinin, 0.1mM phenylmethylsulphonyl fluoride [PMSF]) and centrifuged at 1936 g for 7 min at room temperature. The cell pellets were resuspended in nuclei isolation buffer and again

centrifuged at 1936 g for 7 min at room temperature. The cell pellets were then resuspended in nuclei isolation buffer containing 0.025 % Empigen (nuclei isolation buffer+) and homogenized immediately with ten downward strokes using a tight Dounce-pestle. The cell lysates were centrifuged at 4336 g for 5 min. The nuclei pellets were washed in nuclei isolation buffer+. The nuclei were incubated on ice for 15 min in a series of buffers: HE (10 mM HEPES-NaOH pH 7.5, 1 mM EDTA, and 0.1 mM PMSF), HE + 100 mM NaCl, HE + 500 mM NaCl, HE + 1 M NaCl, and HE + 2 M NaCl. After incubation with salt, centrifugation was performed to separate the nuclear solutions into supernatant and pellet fractions. The proteins in the supernatant fractions were precipitated using 17 % TCA and cold acetone. Both pellets were suspended in sodium dodecyl sulfate-polyacrylamide gel electrophoresis (SDS-PAGE) buffer and subjected to 12.5 % SDS-PAGE and subsequent Coomassie brilliant blue (CBB) staining and western blotting using anti-H2B (Abcam) and anti-HaloTag (Promega) antibodies.

HaloTag labeling

To confirm the expression (Figure 2), H2B-Halo molecules were fluorescently labeled with 100 nM HaloTag TMR Ligand (Promega) overnight at 37°C in 5 % CO_2. Subsequently, the cells were fixed with 1.85 % formaldehyde for 15 min, and then permeabilized with 0.5 % triton for 15 min and stained with 0.5 μg/mL DAPI for 5 min and mounted in PPDI. For single nucleosome imaging, H2B-Halo molecules were fluorescently labeled with 80 pM HaloTag TMR Ligand (Promega) for 20 min at 37°C in 5 % CO_2, washed with Hank's balanced salt saline (HBSS) three times, and then incubated in medium without phenol red for more than 30 min before live cell imaging.

Chemical treatment

For transcriptional inhibition, cells were treated with transcription inhibitors; 100 μM 5, 6-dichlorobenzimidazole-1-β-D-ribofuranoside (DRB) (Sigma-Aldrich) for 2 hr; 100 μg/mL α-amanitin (Sigma-Aldrich) for 2 hr or 20 μg/mL for 6 hr (only for EU labeling); actinomycin D (Sigma-Aldrich) 0.5 μg/mL for 2 hr. To inhibit RNA polymerase I, cells were treated with 1 μM CX5461 (Xcess Biosciences Inc.) for 2 hr. To inhibit splicing, cells were treated with 30 ng/mL Pladienolide B (Santa Cruz) for 2 hr. To degrade mAID-mClover-RPB1 rapidly, cells were incubated in medium supplemented with 1 μg/mL doxycycline (Dox) (BD) for 23 hr and then treated with 500 μM indole-3-acetic acid (IAA) (Nacalai), a natural auxin, in the presence of the Dox for 1 hr. After the treatment, cells were imaged or chemical fixed.

RNA interference

Transfection of siRNA was performed using Lipofectamine RNAiMAX (Invitrogen) according to the manufacturer's instructions. The medium which was transfected to the cells was changed to a flesh medium 16 hr after transfection and the transfected cells were used for subsequent studies 48 hr after transfection. The siRNA oligo targeting CDK9 sequence (Ambion) was used. As a control, an oligo (Invitrogen) was used.

5-ethyl uridine (EU) labeling and quantification

EU incorporation was performed using Click-iT RNA Alexa Fluor 594 Imaging Kit (Invitrogen) according to the manufacturer's instructions. Chemical treated cells were incubated with 500 μM EU for 1 hr during a period of the chemical treatments. The cells were then fixed with 3.7 % formaldehyde for 15 min and permeabilized with 0.5 % Triton X-100 for 15 min. Incorporated EU was labeled by Click-iT reaction according to the

manufacturer's instructions. The cells were stained with 0.5 μg/mL DAPI for 5 min and mounted in PPDI. Image stacks were obtained using the DeltaVision microscopy and projected to cover whole nucleus (7 images). Nucleoplasm regions were extracted on DNA (DAPI) staining. The median of each cell's mean intensity of the nuclear signals after background subtraction (the signals outside nuclei) were calculated and plotted.

Immunoblotting

Cells were lysed in FSB buffer supplemented with 10 % 2-β-mercaptoethanol and incubated at 95 °C for 5 min to denature proteins, followed by sonicated. Then, SDS-PAGE was performed to separate the proteins. Proteins in the gel were transferred to an Immobilon-P membrane (Millipore) and blocked with PBS-T containing 5 % non-fat milk for 30 min at RT. Subsequently, the proteins were incubated with antibodies at the indicated dilutions: anti-histone H2B rabbit polyclonal (Abcam #ab1790) at 1: 10000 or 1:20000, anti-CTD of Rpb1 mouse monoclonal (Abcam #ab817) at 1:1000, anti-α-tubulin mouse monoclonal (Sigma-Aldrich #T6199) at 1:5000, anti-CDK9 mouse monoclonal (Santa Cruz #sc-13130) at 1:500, subsequently incubated with horseradish peroxidase-linked anti-rabbit IgG whole antibody (Bio-Rad) at 1:5000 for anti-H2B, or horseradish peroxidase-linked anti-mouse IgG whole antibody (Bio-Rad) at 1:5000 for anti-CTD and anti-α-tubulin and anti-CDK9. Signal detection was performed using the Immobilon Western Chemiluminescent HRP substrates (Millipore) with a chemiluminescence CCD imaging system, EZ-Capture MG (ATTO).

Immunofluorescence staining

Immunostaining was performed as described previously (Hihara et al., 2012) and all processes were performed at room temperature. Cells were fixed in 1.85 % formaldehyde

(FA; Wako) in PBS for 15 min, and then treated with 50 mM Glycine in 20 mM HEPES (pH 7.5) with 1 mM $MgCl_2$ and 100 mM KCl (HMK) for 5 min, and permeabilized with 0.5 % TritonX-100 (Sigma-Aldrich) in HMK for 5 min. After washing twice with HMK for 5 min, the cells were incubated with 10 % normal goat serum (NGS; Wako) in HMK for 30 min. The cells were incubated with diluted primary antibodies; mouse anti- Ki67 (Oncogene #NA59) at 1:1000, mouse anti-Topoisomerase IIα (MBL #M042-3) at 1:1000, mouse anti-phosphorylated Ser5 of RNA polymerase II (RNAPII-Ser5P provided by Dr. H. Kimura) at 1:1000, rabbit anti-RNAPII-Ser5P (abcam #ab5131) at 1:2000, and mouse anti-RNAPII-Ser2P (Dr. H. Kimura) at 1:1000 or 1:2000 in 1 % NGS in HMK for 1 hr. After washed with 0.5 M NaCl in HMK four times, the cells were incubated with diluted secondary antibodies; goat anti-mouse IgG Alexa 488 (Invitrogen #A11029) at 1:1000, goat anti-mouse IgG Alexa 594 (Invitrogen #A11032) at 1:500 or 1:1000, goat anti-rabbit IgG Alexa 594 (Invitrogen #A11037) at 1:1000, and goat anti-rabbit IgG Alexa 647 (Invitrogen #A21245) at 1:1000 in 1 % NGS in HMK for 1 hr followed by wash with HMK four times. For DNA staining in fixed cells, 0.5 μg/mL DAPI was added to the cells for 5 min followed by washing with HMK. The stained cells were mounted in 10 mM HEPES (pH 7.7) with 2 mM $MgCl_2$, 100 mM KCl, 5 mM EGTA, 78 % glycerol, and paraphenylene diamine (PPDI) and sealed with a rapid epoxy glue (Shiseido). Most of the images were obtained using a DeltaVision microscopy imaging system (Applied Precision) and some (Figures 37 and 38) were acquired with Nikon Eclipse Ti microscope.

Quantification of immunostaining images

Image stacks were obtained using the DeltaVision microscopy. Some images were projected to cover whole nucleus (usually 7 images) and used as a source images. Nucleoplasm regions were extracted based on the DNA (DAPI) staining regions. For

active RNAPII staining, the median of each cell's mean intensity of the nuclear signals after background subtraction (the nuclear signals without primary antibody treatment or the signals outside nuclei) were calculated and plotted. For Ki67 and Topo IIα, the numbers of nuclei with intensity higher than a threshold value were counted and plotted. For signal quantification at nuclear periphery of active RNAPII (Figure 19), the obtained images stacks were deconvolved and projected. The nuclear edge was determined based on the DAPI staining region. A range with a width of 3 pixels, which faces the nuclear edge, was extracted as a nuclear periphery region. The mean intensity in the nuclear periphery was calculated and compared to that in the nucleoplasm as described above.

Total density estimation in the nucleoplasm

I estimated intracellular density distribution from obtained optical path difference (OPD) maps using OI-DIC microscopy as described previously (Imai et al., 2017). Briefly, the following two steps were performed. First, I calculated the refractive index (RI) from the OPD. Because the OPD is proportional to the thickness of a sample and the difference in RI between the sample and the surrounding solution, I calculated the RI of samples on the basis of the RI of the surrounding solution and sample thickness. Second, I obtained the density of the sample from its RI, because the RI of a sample is proportional to its density. The dry mass density in live cells, which consists mainly of proteins and nucleic acids, was calculated from their RI using a single calibration curve (Supplemental Figure S3 in (Imai et al., 2017)). To estimate the densities of the total cell contents, I measured the average thickness of the cytoplasm and nucleus in the cells. To obtain the RI of cytoplasm (RI_{cy}), I used the RI of the surrounding culture medium (RI_{med}, 1.3375). For the RI of the nucleus, I used our calculated values of RI_{cy} and RI_{nuc}, respectively. These

estimates were created using ImageJ software.

Measurements of free Mg^{2+} in the cells

Magnesium Green-AM (ThermoFisher) was applied to the culture medium at 10 μg/mL with 0.02 % Pluronic F-127 (ThermoFisher), and the cells were incubated at 37°C for 1 hr. The cells were then washed twice with Hank's balanced salt saline (HBSS, pH adjusted to 7.4; ThermoFisher) and further incubated in fresh HBSS at 37°C for 15 min to complete hydrolysis of the acetoxymethyl (AM) ester form. Magnesium Green fluorescence was measured by DeltaVision equipped with a 60× objective lens (Olympus) with a FITC filter. The nuclear intensity was measured after subtraction of background signals outside cells and plotted.

Single nucleosome imaging microscopy

Single nucleosomes were observed using an inverted Nikon Eclipse Ti microscope with a 100 mW Sapphire 561-nm laser (Coherent) and sCMOS ORCA-Flash 4.0 camera (Hamamatsu Photonics). Fluorescently labeled H2B-Halo (TMR) in living cells were excited by the 561-nm laser through an objective lens (100× PlanApo TIRF, NA 1.49; Nikon) and detected. An oblique illumination system with TIRF unit (Nikon) was used to excite H2B-Halo (TMR) molecules within a limited thin area in the cell nucleus and reduce a background noise. Sequential image frames were acquired using MataMorph software (Molecular Devices) at a frame rate of 50 ms under continuous illumination. To maintain cell culture conditions (37°C, 5% CO_2, and humidity) under the microscope, a live cell chamber INU-TIZ-F1 (Tokai Hit) and GM-8000 digital gas mixer (Tokai Hit) were used.

Single nucleosome tracking analysis

The methods for image processing, single molecule tracking, and single-nucleosome movement analysis were described previously (Nozaki et al., 2017). Sequential images were converted to 8-bit grayscale and the background noise signals were subtracted with ImageJ software (NIH). The nuclear regions in the images were extracted. Following this step, the centroid of each fluorescent dot in each image was determined and its trajectory was tracked with u-track (MATLAB package) (Jaqaman et al., 2008). To generate PALM images, the individual nucleosome positions were mapped using R software (65 nm/pixel). For single-nucleosome movement analysis, the displacement and mean square displacement (MSD) of the fluorescent dots were calculated based on its trajectory. The originally calculated MSD was in 2D. To obtain the three-dimensional value, the 2D value was multiplied by 1.5 (4 Dt -> 6 Dt). To ascertain the position determination accuracy of the nucleosomes with H2B-Halotag, the standard deviation of two-dimensional movement of immobilized nucleosomes in FA-fixed cells (/50 ms, n = 10 molecules) were calculated. To make the heat map of chromatin dynamics, the median nucleosome movements (during 50 ms) in 3 × 3 pixels (65 nm/pixel) were plotted with a color scale from blue to red using R.

RNA preparation and quantitative real-time PCR

Sample RNA purification was performed by using the Click-iT Nascent RNA Capture Kit (Invitrogen). To label the nascent RNA with 5-ethynyl-uridine (5-EU), cells cultured on 6 wells were incubated with DMEM supplemented with 500 μM of 5-EU for 1 hr at 37°C 5% CO_2. After labeling, RNA was extracted from the cells by using TRIzol (Invitrogen) and subsequently labeled RNA was biotinylated by the click reaction. The biotinylated

RNA was purified by streptavidin beads. To prepare cDNA, the purified RNA was reverse transcribed using Super ScriptTM III First-Strand Synthesis SuperMix (Invitrogen), then *CDK6* gene region was amplified from templated the purified cDNA using TB Green™ Premix Ex Taq ™ (Takara) and simultaneously SYBR Green signal was detected using an equipment Thermal Cycler Dice Real Time System TP800 (Takara). 18S rDNA was used as a reference gene. Primers were shown in below.

h18S rDNA_Fw: 5'-GTTGGTGGAGCGATTTGTCTGGTT-3'

h18S rDNA_Rv: 5'-TATTGCTCAATCTCGGGTGGCTGA-3'

hCDK6_Int2_Fw: 5'-TGCAGCTGTGCAACTTAGA-3'

hCDK6_Int2_Rv: 5'-GTTGGCTTATCCTGTCCCTAAA-3'

hCDK6_Ex2-3 spliced_Fw: 5'-ATGCCGCTCTCCACCAT-3'

hCDK6_Ex2-3 spliced_Rv: 5'-ACATCAAACAACCTGAC-3'

Acknowledgements

This research would not have been possible without great help from many people. At first I would like to express my deepest gratitude to my supervisor Prof. Kazuhiro Maeshima and Assistant Prof. Kayo Hibino for their excellent guidance, kind encouragement, and providing me with original philosophy for research. Their attitude for science inspires my feeling of respect.

For the help for the research, I would like to thank many people: Prof. Masato T. Kanemaki (National Institute of Genetics) and Assistant Prof. Toyoaki Natsume (National Institute of Genetics) for providing AID materials and experimental methods; Prof. Hiroshi Kimura (Tokyo Institute of Technology) and Prof. Kyoji Horie (Nara Medical University) for providing research materials; Associate Prof. Daisuke Kaida (Toyama University) for helpful suggestions about splicing inhibition; Dr. Michael Shribak (Marine Biological Laboratory) for developing the OI-DIC microscope and giving me a chance to perform experiments with the microscope in his laboratory; Dr. Tomomi Tani (Marine Biological Laboratory) for supporting experimental equipment during I studied at Dr. Michael's Lab.

Through my Ph.D. course, my committee members, Prof. Hiroyuki Araki, Prof Ituro Inoue, Prof. Masato T. Kanemaki, and Prof. Kuniaki Saito in National Institute of Genetics/SOKENDAI, and Prof. Yuki Yamaguchi in Tokyo Institute of Technology, always gave me helpful advices and supports. And Dr. Susumu Hirose (National Institute of Genetics), Dr. Yasushi Hiromi (National Institute of Genetics), and Dr. Hiroaki Seino (National Institute of Genetics) kindly made meaningful discussions on my study. I would

like to thank them very much.

I would also like to thank the members of Maeshima laboratory in National Institute of Genetics/SOKENDAI, Assistant Prof. Satoru Ide, Dr. Tadasu Nozaki, Dr. Ryosuke Imai, Dr. Michael Babokhov, Dr. Eloise I. Prieto, Ms. Sachiko Tamura, Ms. Asuka Sasaki, Ms. Mai Tambo, Mr. Tomohiro Yamaguchi, Ms. Hiroko Ochi, and Ms. Kaeko Nakaguchi for helpful discussions, technical assistances, and kind encouragements.

In addition, I would like to thank Prof. Yukio Ishimi and members in his laboratory in Ibaraki University for giving me a chance to move to Maeshima Laboratory when I was an undergraduate student.

Finally, I would like to thank my family and relatives, especially my parents Yoshihisa and Shizuko and my sister Yuka and my brother Yuki and my grandmother Takeko for their continuous support and encouragement through my life.

The study in this thesis was supported by Japan Society for the Promotion of Science (JSPS), Japan Science and Technology Agency (JST) CREST, and the SOKENDAI Short-Stay Study Abroad Program in fiscal year 2017.

References

Albiez, H., Cremer, M., Tiberi, C., Vecchio, L., Schermelleh, L., Dittrich, S., Kupper, K., Joffe, B., Thormeyer, T., von Hase, J., Yang, S., Rohr, K., Leonhardt, H., Solovei, I., Cremer, C., Fakan, S., Cremer, T. (2006). Chromatin domains and the interchromatin compartment form structurally defined and functionally interacting nuclear networks. *Chromosome Res* **14**, 707-733.

Baddeley, D., Chagin, V.O., Schermelleh, L., Martin, S., Pombo, A., Carlton, P.M., Gahl, A., Domaing, P., Birk, U., Leonhardt, H., Cremer, C., Cardoso, M.C. (2010). Measurement of replication structures at the nanometer scale using super-resolution light microscopy. *Nucleic acids research* **38**, e8.

Belmont, A.S., and Bruce, K. (1994). Visualization of G1 chromosomes: a folded, twisted, supercoiled chromonema model of interphase chromatid structure. *The Journal of cell biology* **127**, 287-302.

Bensaude, O. (2011). Inhibiting eukaryotic transcription: Which compound to choose? How to evaluate its activity? *Transcription* **2**, 103-108.

Berezney, R., Dubey, D.D., and Huberman, J.A. (2000). Heterogeneity of eukaryotic replicons, replicon clusters, and replication foci. *Chromosoma* **108**, 471-484.

Betzig, E., Patterson, G.H., Sougrat, R., Lindwasser, O.W., Olenych, S., Bonifacino, J.S., Davidson, M.W., Lippincott-Schwartz, J., and Hess, H.F. (2006). Imaging intracellular fluorescent proteins at nanometer resolution. *Science (New York, NY)* **313**, 1642-1645.

Bickmore, W.A. (2013). The spatial organization of the human genome. *Annu Rev Genomics Hum Genet* **14**, 67-84.

Bodnar, A.G., Ouellette, M., Frolkis, M., Holt, S.E., Chiu, C.P., Morin, G.B., Harley, C.B., Shay, J.W., Lichtsteiner, S., and Wright, W.E. (1998). Extension of life-span by introduction of telomerase into normal human cells. *Science (New York, NY)* **279**, 349-352.

Boettiger, A.N., Bintu, B., Moffitt, J.R., Wang, S., Beliveau, B.J., Fudenberg, G., Imakaev,

M., Mirny, L.A., Wu, C.T., and Zhuang, X. (2016). Super-resolution imaging reveals distinct chromatin folding for different epigenetic states. *Nature* **529**, 418-422.

Buckley, M.S., and Lis, J.T. (2014). Imaging RNA Polymerase II transcription sites in living cells. *Curr Opin Genet Dev* **25**, 126-130.

Bushnell, D.A., Cramer, P., and Kornberg, R.D. (2002). Structural basis of transcription: alpha-amanitin-RNA polymerase II cocrystal at 2.8 Å resolution. *Proceedings of the National Academy of Sciences of the United States of America* **99**, 1218-1222.

Cardoso, M.C., Schneider, K., Martin, R.M., and Leonhardt, H. (2012). Structure, function and dynamics of nuclear subcompartments. *Curr Opin Cell Biol* **24**, 79-85.

Chen, B., Gilbert, L.A., Cimini, B.A., Schnitzbauer, J., Zhang, W., Li, G.W., Park, J., Blackburn, E.H., Weissman, J.S., Qi, L.S., Huang, B. (2013). Dynamic imaging of genomic loci in living human cells by an optimized CRISPR/Cas system. *Cell* **155**, 1479-1491.

Chen, C., Lim, H.H., Shi, J., Tamura, S., Maeshima, K., Surana, U., and Gan, L. (2016). Budding yeast chromatin is dispersed in a crowded nucleoplasm in vivo. *Molecular biology of the cell* **27**, 3357-3368.

Cheung, T.H., and Rando, T.H. (2013). Molecular regulation of stem cell quiescence. *Nat Rev Mol Cell Biol* **14**, 329-340.

Cho, W.K., Jayanth, N., English, B.P., Inoue, T., Andrews, J.O., Conway, W., Grimm, J.B., Spille, J.H., Lavis, L.D., Lionnet, T., Cisse, I.I. (2016). RNA Polymerase II cluster dynamics predict mRNA output in living cells. *eLife* **5**, e13617.

Cho, W.K., Spille, J.H., Hecht, M., Lee, C., Li, C., Grube, V., and Cisse, I.I. (2018). Mediator and RNA polymerase II clusters associate in transcription-dependent condensates. *Science (New York, NY)* **361**, 412-415.

Chong, S., Dugast-Darzacq, C., Liu, Z., Dong, P., Dailey, G.M., Cattoglio, C., Heckert, A., Banala, S., Lavis, L., Darzacq, X., Tjian, R. (2018). Imaging dynamic and selective low-complexity domain interactions that control gene transcription. *Science (New York,*

NY) **361**, eaar2555.

Chubb, J.R., Boyle, S., Perry, P., and Bickmore, W.A. (2002). Chromatin motion is constrained by association with nuclear compartments in human cells. *Current biology : CB* **12**, 439-445.

Cisse, I.I., Izeddin, I., Causse, S.Z., Boudarene, L., Senecal, A., Muresan, L., Dugast-Darzacq, C., Hajj, B., Dahan, M., and Darzacq, X. (2013). Real-time dynamics of RNA polymerase II clustering in live human cells. *Science (New York, NY)* **341**, 664-667.

Cseresnyes, Z., Schwarz, U., and Green, C.M. (2009). Analysis of replication factories in human cells by super-resolution light microscopy. *BMC Cell Biol* **10**, 88.

Dekker, J., and Heard, E. (2015). Structural and functional diversity of Topologically Associating Domains. *FEBS Lett* **589**, 2877-2884.

Dion, V., and Gasser, S.M. (2013). Chromatin movement in the maintenance of genome stability. *Cell* **152**, 1355-1364.

Dixon, J.R., Selvaraj, S., Yue, F., Kim, A., Li, Y., Shen, Y., Hu, M., Liu, J.S., and Ren, B. (2012). Topological domains in mammalian genomes identified by analysis of chromatin interactions. *Nature* **485**, 376-380.

Djebali, S., Davis, C.A., Merkel, A., Dobin, A., Lassmann, T., Mortazavi, A., Tanzer, A., Lagarde, J., Lin, W., Schlesinger, F., et al. (2012). Landscape of transcription in human cells. *Nature* **489**, 101-108.

Drygin, D., Lin, A., Bliesath, J., Ho, C.B., O'Brien, S.E., Proffitt, C., Omori, M., Haddach, M., Schwaebe, M.K., Siddiqui-Jain, A., Streiner, N., Quin, J.E., Sanij, E., Bywater, M.J., Hannan, R.D., Ryckman, D., Anderes, K., Rice, W.G. (2011). Targeting RNA polymerase I with an oral small molecule CX-5461 inhibits ribosomal RNA synthesis and solid tumor growth. *Cancer research* **71**, 1418-1430.

Eagen, K.P., Hartl, T.A., and Kornberg, R.D. (2015). Stable Chromosome Condensation Revealed by Chromosome Conformation Capture. *Cell* **163**, 934-946.

Eltsov, M., Maclellan, K.M., Maeshima, K., Frangakis, A.S., and Dubochet, J. (2008). Analysis of cryo-electron microscopy images does not support the existence of 30-nm chromatin fibers in mitotic chromosomes in situ. *Proceedings of the National Academy of Sciences of the United States of America* **105**, 19732-19737.

Feuerborn, A., and Cook, P.R. (2015). Why the activity of a gene depends on its neighbors. *Trends in genetics : TIG* **31**, 483-490.

Fussner, E., Strauss, M., Djuric, U., Li, R., Ahmed, K., Hart, M., Ellis, J., and Bazett-Jones, D.P. (2012). Open and closed domains in the mouse genome are configured as 10-nm chromatin fibres. *EMBO Rep* **13**, 992-996.

Germier, T., Kocanova, S., Walther, N., Bancaud, A., Shaban, H.A., Sellou, H., Politi, A.Z., Ellenberg, J., Gallardo, F., and Bystricky, K. (2017). Real-Time Imaging of a Single Gene Reveals Transcription-Initiated Local Confinement. *Biophysical journal* **113**, 1383-1394.

Ghamari, A., van de Corput, M.P., Thongjuea, S., van Cappellen, W.A., van Ijcken, W., van Haren, J., Soler, E., Eick, D., Lenhard, B., and Grosveld, F.G. (2013). In vivo live imaging of RNA polymerase II transcription factories in primary cells. *Genes & development* **27**, 767-777.

Gu, B., Swigut, T., Spencley, A., Bauer, M.R., Chung, M., Meyer, T., and Wysocka, J. (2018). Transcription-coupled changes in nuclear mobility of mammalian cis-regulatory elements. *Science (New York, NY)* **359**, 1050-1055.

Hajjoul, H., Mathon, J., Ranchon, H., Goiffon, I., Mozziconacci, J., Albert, B., Carrivain, P., Victor, J.M., Gadal, O., Bystricky, K., Bancaud, A. (2013). High-throughput chromatin motion tracking in living yeast reveals the flexibility of the fiber throughout the genome. *Genome Res* **23**, 1829-1838.

Hansen, J.C. (2002). Conformational dynamics of the chromatin fiber in solution: determinants, mechanisms, and functions. *Annu Rev Biophys Biomol Struct* **31**, 361-392.

Heun, P., Laroche, T., Shimada, K., Furrer, P., and Gasser, S.M. (2001). Chromosome dynamics in the yeast interphase nucleus. *Science (New York, NY)* **294**, 2181-2186.

Hihara, S., Pack, C.G., Kaizu, K., Tani, T., Hanafusa, T., Nozaki, T., Takemoto, S., Yoshimi, T., Yokota, H., Imamoto, N., Sako, Y., Kinjo, M., Takahashi, K., Nagai, T., and Maeshima, K. (2012). Local nucleosome dynamics facilitate chromatin accessibility in living mammalian cells. *Cell reports* **2**, 1645-1656.

Hsieh, T.H., Weiner, A., Lajoie, B., Dekker, J., Friedman, N., and Rando, O.J. (2015). Mapping Nucleosome Resolution Chromosome Folding in Yeast by Micro-C. *Cell* **162**, 108-119.

Hu, Y., Kireev, I., Plutz, M., Ashourian, N., and Belmont, A.S. (2009). Large-scale chromatin structure of inducible genes: transcription on a condensed, linear template. *The Journal of cell biology* **185**, 87-100.

Hubner, M.R., Eckersley-Maslin, M.A., and Spector, D.L. (2013). Chromatin organization and transcriptional regulation. *Curr Opin Genet Dev* **23**, 89-95.

Imai, R., Nozaki, T., Tani, T., Kaizu, K., Hibino, K., Ide, S., Tamura, S., Takahashi, K., Shribak, M., and Maeshima, K. (2017). Density imaging of heterochromatin in live cells using orientation-independent-DIC microscopy. *Molecular biology of the cell* **28**, 3349-3359.

Jackson, D.A., and Pombo, A. (1998). Replicon clusters are stable units of chromosome structure: evidence that nuclear organization contributes to the efficient activation and propagation of S phase in human cells. *The Journal of cell biology* **140**, 1285-1295.

Jaqaman, K., Loerke, D., Mettlen, M., Kuwata, H., Grinstein, S., Schmid, S.L., and Danuser, G. (2008). Robust single-particle tracking in live-cell time-lapse sequences. *Nat Methods* **5**, 695-702.

Kimura, H., and Cook, P.R. (2001). Kinetics of core histones in living human cells: little exchange of H3 and H4 and some rapid exchange of H2B. *The Journal of cell biology* **153**, 1341-1353.

Kimura, H., Sugaya, K., and Cook, P.R. (2002). The transcription cycle of RNA polymerase II in living cells. *The Journal of cell biology* **159**, 777-782.

Kireeva, N., Lakonishok, M., Kireev, I., Hirano, T., and Belmont, A.S. (2004). Visualization of early chromosome condensation: a hierarchical folding, axial glue model of chromosome structure. *The Journal of cell biology* **166**, 775-785.

Koga, M., Hayashi, M., and Kaida, D. (2015). Splicing inhibition decreases phosphorylation level of Ser2 in Pol II CTD. *Nucleic acids research* **43**, 8258-8267.

Kwak, H., and Lis, J.T. (2013). Control of transcriptional elongation. *Annual review of genetics* **47**, 483-508.

Lemaitre, C., and Bickmore, W.A. (2015). Chromatin at the nuclear periphery and the regulation of genome functions. *Histochem Cell Biol* **144**, 111-122.

Levi, V., Ruan, Q., Plutz, M., Belmont, A.S., and Gratton, E. (2005). Chromatin dynamics in interphase cells revealed by tracking in a two-photon excitation microscope. *Biophysical journal* **89**, 4275-4285.

Lieberman-Aiden, E., van Berkum, N.L., Williams, L., Imakaev, M., Ragoczy, T., Telling, A., Amit, I., Lajoie, B.R., Sabo, P.J., Dorschner, M.O., Sandstrom, R., Bernstein, B., Bender, M.A., Groudine, M., Gnirke, A., Stamatoyannopoulos, J., Mirny, L.A., Lander, E.S., Dekker, J. (2009). Comprehensive mapping of long-range interactions reveals folding principles of the human genome. *Science (New York, NY)* **326**, 289-293.

Lu, H., Yu, D., Hansen, A.S., Ganguly, S., Liu, R., Heckert, A., Darzacq, X., and Zhou, Q. (2018). Phase-separation mechanism for C-terminal hyperphosphorylation of RNA polymerase II. *Nature* **558**, 318-323.

Luger, K., Mader, A.W., Richmond, R.K., Sargent, D.F., and Richmond, T.J. (1997). Crystal structure of the nucleosome core particle at 2.8 Å resolution. *Nature* **389**, 251-260.

Ma, H., Tu, L.C., Naseri, A., Huisman, M., Zhang, S., Grunwald, D., and Pederson, T. (2016). Multiplexed labeling of genomic loci with dCas9 and engineered sgRNAs using CRISPRainbow. *Nat Biotechnol* **34**, 528-530.

Maeshima, K., Hihara, S., and Eltsov, M. (2010a). Chromatin structure: does the 30-nm fibre exist in vivo? *Curr Opin Cell Biol* **22**, 291-297.

Maeshima, K., Iino, H., Hihara, S., Funakoshi, T., Watanabe, A., Nishimura, M., Nakatomi, R., Yahata, K., Imamoto, F., Hashikawa, T., Yokota, H., Imamoto, N. (2010b). Nuclear pore formation but not nuclear growth is governed by cyclin-dependent kinases (Cdks) during interphase. *Nat Struct Mol Biol* **17**, 1065-1071.

Maeshima, K., Matsuda, T., Shindo, Y., Imamura, H., Tamura, S., Imai, R., Kawakami, S., Nagashima, R., Soga, T., Noji, H., Oka, K., Nagai, T. (2018). A Transient Rise in Free Mg^{2+} Ions Released from ATP-Mg Hydrolysis Contributes to Mitotic Chromosome Condensation. *Current biology : CB* **28**, 444-451 e446.

Maeshima, K., Rogge, R., Tamura, S., Joti, Y., Hikima, T., Szerlong, H., Krause, C., Herman, J., Seidel, E., DeLuca, J., Ishikawa, T., Hansen, J.C. (2016). Nucleosomal arrays self-assemble into supramolecular globular structures lacking 30-nm fibers. *EMBO J* **35**, 1115-1132.

Markaki, Y., Gunkel, M., Schermelleh, L., Beichmanis, S., Neumann, J., Heidemann, M., Leonhardt, H., Eick, D., Cremer, C., and Cremer, T. (2010). Functional nuclear organization of transcription and DNA replication: a topographical marriage between chromatin domains and the interchromatin compartment. *Cold Spring Harb Symp Quant Biol* **75**, 475-492.

Marshall, W.F., Straight, A., Marko, J.F., Swedlow, J., Dernburg, A., Belmont, A., Murray, A.W., Agard, D.A., and Sedat, J.W. (1997). Interphase chromosomes undergo constrained diffusional motion in living cells. *Current biology : CB* **7**, 930-939.

Nagano, T., Lubling, Y., Varnai, C., Dudley, C., Leung, W., Baran, Y., Mendelson Cohen, N., Wingett, S., Fraser, P., and Tanay, A. (2017). Cell-cycle dynamics of chromosomal organization at single-cell resolution. *Nature* **547**, 61-67.

Natsume, T., Kiyomitsu, T., Saga, Y., and Kanemaki, M.T. (2016). Rapid Protein Depletion in Human Cells by Auxin-Inducible Degron Tagging with Short Homology Donors. *Cell reports* **15**, 210-218.

Nguyen, V.T., Giannoni, F., Dubois, M.F., Seo, S.J., Vigneron, M., Kedinger, C., and Bensaude, O. (1996). In vivo degradation of RNA polymerase II largest subunit triggered by alpha-amanitin. *Nucleic acids research* **24**, 2924-2929.

Nora, E.P., Lajoie, B.R., Schulz, E.G., Giorgetti, L., Okamoto, I., Servant, N., Piolot, T., van Berlum, N.L., Meisig, J., Sedat, J.W., Gribnau, J., Barillot, E., Blüthgen, N., Dekker, J., Heard, E. (2012). Spatial partitioning of the regulatory landscape of the X-inactivation centre. *Nature* **485**, 381-385.

Nozaki, T., Imai, R., Tanbo, M., Nagashima, R., Tamura, S., Tani, T., Joti, Y., Tomita, M., Hibino, K., Kanemaki, M.T., Wendt, K.S., Okada, Y., Nagai, T., Maeshima, K. (2017). Dynamic Organization of Chromatin Domains Revealed by Super-Resolution Live-Cell Imaging. *Mol Cell* **67**, 282-293 e287.

Ochiai, H., Sugawara, T., and Yamamoto, T. (2015). Simultaneous live imaging of the transcription and nuclear position of specific genes. *Nucleic acids research* **43**, e127.

Ou, H.D., Phan, S., Deerinck, T.J., Thor, A., Ellisman, M.H., and O'Shea, C.C. (2017). ChromEMT: Visualizing 3D chromatin structure and compaction in interphase and mitotic cells. *Science (New York, NY)* **357**, eaag0025.

Rao, S.S., Huntley, M.H., Durand, N.C., Stamenova, E.K., Bochkov, I.D., Robinson, J.T., Sanborn, A.L., Machol, I., Omer, A.D., Lander, E.S., Aiden, E.L. (2014). A 3D map of the human genome at kilobase resolution reveals principles of chromatin looping. *Cell* **159**, 1665-1680.

Rao, S.S.P., Huang, S.C., Glenn St Hilaire, B., Engreitz, J.M., Perez, E.M., Kieffer-Kwon, K.R., Sanborn, A.L., Johnstone, S.E., Bascom, G.D., Bochkov, I.D., et al. (2017). Cohesin Loss Eliminates All Loop Domains. *Cell* **171**, 305-320 e324.

Ricci, M.A., Manzo, C., Garcia-Parajo, M.F., Lakadamyali, M., and Cosma, M.P. (2015). Chromatin fibers are formed by heterogeneous groups of nucleosomes in vivo. *Cell* **160**, 1145-1158.

Risca, V.I., Denny, S.K., Straight, A.F., and Greenleaf, W.J. (2017). Variable chromatin structure revealed by in situ spatially correlated DNA cleavage mapping. *Nature* **541**,

237-241.

Rust, M.J., Bates, M., and Zhuang, X.W. (2006). Sub-diffraction-limit imaging by stochastic optical reconstruction microscopy (STORM). *Nature Methods* **3**, 793-795.

Sabari, B.R., Dall'Agnese, A., Boija, A., Klein, I.A., Coffey, E.L., Shrinivas, K., Abraham, B.J., Hannett, N.M., Zamudio, A.V., Manteiga, J.C., et al. (2018). Coactivator condensation at super-enhancers links phase separation and gene control. *Science (New York, NY)* **361**, eaar3958.

Sanborn, A.L., Rao, S.S., Huang, S.C., Durand, N.C., Huntley, M.H., Jewett, A.I., Bochkov, I.D., Chinnappan, D., Cutkosky, A., Li, J., Geeting, K.P., Gnirke, A., Melnikov, A., McKenna, D., Stamenova, E.K., Lander, E.S., Aiden, E.L. (2015). Chromatin extrusion explains key features of loop and domain formation in wild-type and engineered genomes. *Proceedings of the National Academy of Sciences of the United States of America* **112**, E6456-6465.

Selvin, P.R., Lougheed, T., Tonks Hoffman, M., Park, H., Balci, H., Blehm, B.H., and Toprak, E. (2007). Fluorescence Imaging with One-Nanometer Accuracy (FIONA). *CSH Protoc* **2007**, pdb top27.

Sexton, T., Yaffe, E., Kenigsberg, E., Bantignies, F., Leblanc, B., Hoichman, M., Parrinello, H., Tanay, A., and Cavalli, G. (2012). Three-Dimensional Folding and Functional Organization Principles of the Drosophila Genome. *Cell* **148**, 458-472.

Shinkai, S., Nozaki, T., Maeshima, K., and Togashi, Y. (2016). Dynamic nucleosome movement tells Structural information of topological chromatin domains in human cells. *PLoS Computational Biology* **12**, e1005136.

Smallwood, A., and Ren, B. (2013). Genome organization and long-range regulation of gene expression by enhancers. *Curr Opin Cell Biol* **25**, 387-394.

Stasevich, T.J., Hayashi-Takanaka, Y., Sato, Y., Maehara, K., Ohkawa, Y., Sakata-Sogawa, K., Tokunaga, M., Nagase, T., Nozaki, N., McNally, J.G., Kimura, H. (2014). Regulation of RNA polymerase II activation by histone acetylation in single living cells. *Nature* **516**, 272-275.

Subach, F.V., Patterson, G.H., Manley, S., Gillette, J.M., Lippincott-Schwartz, J., and Verkhusha, V.V. (2009). Photoactivatable mCherry for high-resolution two-color fluorescence microscopy. *Nature Methods* **6**, 153-159.

Szabo, Q., Jost, D., Chang, J.M., Cattoni, D.I., Papadopoulos, G.L., Bonev, B., Sexton, T., Gurgo, J., Jacquier, C., Nollmann, M., Bantignies, F., Cavalli, G. (2018). TADs are 3D structural units of higher-order chromosome organization in Drosophila. *Sci Adv* **4**, eaar8082.

Tokunaga, M., Imamoto, N., and Sakata-Sogawa, K. (2008). Highly inclined thin illumination enables clear single-molecule imaging in cells. *Nat Methods* **5**, 159-161.

Van Steensel, B., and Belmont, A.S. (2017). Lamina-Associated Domains: Links with Chromosome Architecture, Heterochromatin, and Gene Repression. *Cell* **169**, 780-791.

Vian, L., Pekowska, A., Rao, S.S.P., Kieffer-Kwon, K.R., Jung, S., Baranello, L., Huang, S.C., El Khattabi, L., Dose, M., Pruett, N., et al. (2018). The Energetics and Physiological Impact of Cohesin Extrusion. *Cell* **173**, 1165-1178.e1120.

Xiang, W., Roberti, M.J., Heriche, J.K., Huet, S., Alexander, S., and Ellenberg, J. (2018). Correlative live and super-resolution imaging reveals the dynamic structure of replication domains. *The Journal of cell biology* **217**, 1973-1984.

Yesbolatova, A., T. Natsume, K. Hayashi, and M.T. Kanemaki. (2019). Generation of conditional auxin-inducible degron (AID) cells and tight control of degron-fused proteins using the degradation inhibitor auxinole. *bioRxiv* doi.org/10.1101/530410 (Preprint Posted January 26, 2019)